UNIVERSITY OF SOUTHAMPTON

Heavy-Light Hadron Matrix Elements from Lattice QCD

by

Victor Isaac Lesk

A thesis submitted for the degree of

Doctor of Philosophy

Department of Physics and Astronomy

August 29, 2000

UNIVERSITY OF SOUTHAMPTON

ABSTRACT

FACULTY OF SCIENCE

PHYSICS

Doctor of Philosophy

Heavy-Light Hadron Matrix Elements from Lattice QCD

Victor Isaac Lesk

Two point and three point correlation functions are calculated from a lattice simulation at two values of the bare coupling. Light-light and heavy-light meson masses, decay constants and semileptonic form factors are extracted. Guided extrapolations are performed to estimate the masses, decay constants and form factors of physical particles. Approximation methods are identified and systematic errors are quantified and discussed.

Contents

List of Figures

List of Tables

Acknowledgements

Primary acknowledgement and thanks must go to my supervisor Jonathan Flynn, who has taught me many new things. My principal colleague Chris Maynard is acknowledged for his persistence and flair. Giulia de Divitiis, Luigi del Debbio, James Gill, Giuseppe Lacagnina, Laurent Lellouch and Juan Nieves have all been a pleasure to work with. I have been privileged to be in osmotic contact with Chris Sachrajda and his students Chris Dawson, Alex Dougall and Massimo di Pierro, and with David Lin who is extremely good company. Thanks also to the other members of staff and students in the group for their stimulating contribution. Thanks to Mike Hill for maintaining the computer systems on which this work has depended. Also thanks to Kevin Anderson, my very first contact in Southampton, for showing me the ropes. Finally a very special thank you to my family.

Chapter 1

Introduction

This thesis presents results from a simulation of heavy-light meson physics using lattice-regularized quenched QCD with input from heavy-light meson chiral perturbation theory and heavy quark effective theory. The hadronic parts of the matrix elements for the semileptonic decays $B \to \pi$, $B \to \rho$, $D \to K$, $D \to K^*$, $D \to \pi$ and $D \to \rho$ are calculated, and the conventional form factors are presented for these decays. Theoretical estimates for the differential decay rate for these processes are obtained and compared to experiment where a measurement is available. Theoretical estimates of $|V_{cs}|$, $|V_{cd}|$ and $|V_{ub}|$ are given. Theoretical estimates of the decay constants f_B, f_{B_s}, f_{B^*}, $f_{B_s^*}$, f_D, f_{D_s}, f_{D^*}, $f_{D_s^*}$, f_K, f_{K^*}, f_π and f_ρ (as defined by Eq^{ns} 3.5 and 3.6) are determined. All dimensionful quantities require knowledge of the lattice spacing a, which is defined from the gluonic force scale r_0 following Refs. [1] and [2]. The charm and bottom mass scales are set by the lightest c/b meson masses, the D and the B ($I(J^P) = \frac{1}{2}(0^-)$) respectively, except in the case of decay constants, where the mass of the decaying meson is used.

The remainder of this introduction contains an overview of the field. Chapter 2

contains an introduction to QCD field theory and its lattice analogue. Chapter 3 details the procedure for estimating matrix elements of weak currents between single-particle states from lattice QCD. There then follows a presentation of the results, predictions for semileptonic decay rates (chapter 4) and decay constants (chapter 5), which includes a test of some of the relations between matrix elements arising from additional symmetries of QCD in the heavy quark and chiral limits. A systematic discussion of the approximations and uncertainties follows in chapter 7. Conclusions are presented in chapter 8. An appendix is provided detailing definitions, conventions and formulae, as well as a list of experimental inputs, and a representative set of lattice results.

1.1 Current Progress in Heavy Flavour Particle Experiments

1.1.1 Semileptonic B Decays to Light Flavours

As of October 1999, the Cornell Electron Storage Ring is running a new experiment with the centre-of-mass energy of the beam tuned to the $\Upsilon(4S)$ resonance at 10.58(4) GeV [3], the threshold above which $B\overline{B}$ creation becomes energetically possible. This experiment will be at higher luminosity than previous resonant $B\overline{B}$ experimental runs, which have created some 10 million $B\overline{B}$ events between them. The data from these completed runs have been used to infer the total decay rate for $B \to \pi l \nu_l$, $B \to \rho l \nu_l$ and $B \to \omega l \nu_l$ [4], and the differential decay rate for $B \to \rho$ is soon to be published [5]. The methods and results of the CLEO collaboration are summarized in Ref. [6]. The region of the Dalitz plot probed with smallest systematic uncertainty is that of high lepton energy $E_l > 2.3$ GeV, relative to which the lepton rest masses are negligible. Pole-dominance models [7]

are then used to extend the the range of the results in q^2 allowing the integrated semileptonic decay rate to be estimated. Alternatively, the product of the total lifetime and the semileptonic branching ratio can be used. The semileptonic rates for $B \to \pi$ and $B \to \rho$ lead to independent estimates for $|V_{ub}|$, which lie in the interval $(2.5 - 4.0) \times 10^{-3}$.

1.1.2 Semileptonic D Decays to Light Flavours

Experiments with a D Physics programme include FOCUS (Fermilab), and the CLEO detector at CESR. Form factors for $D \to Kl\nu_l$ are measured over the entire kinematic range of q^2 with reasonable accuracy. In his review at the Heavy Flavours 8 conference, Stanton [8] claims that the best results remain those of 1995 and before (from FNAL E687, Ref. [9, 10]). Measurement of $D \to \pi l\nu_l$ is more difficult due to Cabibbo suppression, but Ref.[8] cites an imminent measurement from FOCUS which will draw on ~ 100 times as many events as in past efforts.

1.1.3 Decay constants

Heavy-light decay constants are not of primary interest, and there have been few experiments directed towards their measurement. Only f_{D_s} has been well studied, with the most recent determinations from the CLEO detector, BEATRICE2K and the Aleph collaboration at CERN (Ref. [11, 12]); a more complete synopsis is given in Ref. [13]. However, there are important phenomenological applications for decay constants; the combination $f_B\sqrt{B_B}$, for both B_d and B_s mesons, needs to be known for extracting CKM and CP-violating parameters (the parameter B_B describes $B\overline{B}$ mixing, and is expected to be close to unity). Decay constants are also popular as easily calculable tests of new simulation methods within the

lattice community.

1.2 Theoretical Background

The standard model of particle physics is a quantum field theory containing 3 gauge symmetries, whose vector bosons carry the fundamental strong and electroweak forces. At low energies the electroweak gauge symmetry is broken by the vacuum, leading to massive weak vector bosons ($W^{\pm}$,Z^0) and the massless photon (γ) which couples only to electric current. The matter fields are 6 flavours of coloured, charged fermions (q), 6 fermions which have no colour (l) and the symmetry-breaking scalar (H). The colour force, mediated by gluons (g) is confining and the spectrum of the standard model at long distances contains colourless bound states and resonances $q\bar{q}$ and qqq. In this work, the colour sector of the standard model, the theory of quantum chromodynamics (QCD), is simulated on a spacetime lattice, with effective operators used for weak current interactions. The path integral formulation is adopted [14]. A coordinate rotation to imaginary time is performed [15], which permits stochastic evaluation of the amplitude for a decay. The sum over configurations of the fermionic fields is performed on each gauge configuration using a closed-form expression (*cf.* Eq$^{\text{n}}$ 2.9).

The lattice method of calculating amplitudes in QCD dates from the late 1970's [16], and is now widely consulted as a means of predicting strong interaction matrix elements. In general, the QCD action starts with Poincaré, gauge and chiral symmetries; on the introduction of a lattice, the action necessarily loses Poincaré symmetry, which on a finite lattice is also broken by the boundaries. The gauge symmetry, by contrast, may be explicitly retained. Chiral symmetry may be retained only if one is prepared to lose correspondence with some of the original particle content [17]. However, the freedom to choose any of the infinitely many

discretisations of the QCD action can be used to mitigate the consequences of this 'no-go' theorem. Current efforts in lattice QCD can be classified according to their discretisation scheme for the action. The Wilson action(*cf.* Chap. 2) breaks chiral symmetry explicitly with a second-derivative term, and has the advantage of being amenable to systematic improvement; only one operator of dimension 5 needs to be added to tune the action to remove terms of order a in spectral quantities, and operator improvement is also relatively simple. The staggered formulation [18] retains a subgroup of the original symmetry, at the cost of distributing the components of each spinor field over neigbouring sites. Algorithms for staggered fermions are practical for somewhat lower masses than in the Wilson case. There are technical complications relating to flavour symmetry in the staggered formulation. In this work, Wilson fermions are used.

The consequences for matrix elements of the explicit breaking of chiral symmetry are not well understood; this question has prompted the development of actions in which chiral symmetry breaking is handled in a more sophisticated way. In the Ginsparg-Wilson formulation, the action is constructed to satisfy a relation at any lattice spacing which develops into chiral symmetry at $a = 0$. Actions satisfying the Ginsparg-Wilson relation are currently computationally expensive, and are not used in this work.

Practicioners of lattice QCD are currently struggling with the problems of simulating processes with two or more hadrons in the final state, and of calculating matrix elements of processes involving light quarks, where conventional algorithms slow down critically.

Another widespread technique for estimating matrix elements for hadronic processes utilises sum rules arising from the operator product expansion [19] of light-cone perturbation theory [20]. The light-cone sum rule approach has a different set of strengths and weaknesses. Although formulated in the continuum, it re-

quires many poorly determined inputs including the quark and gluon condensates. Quark model calculations have also been used [21, 22].

Chapter 2

Lattice Methods of QCD Calculations

The substantial part of this work consists in calculating the Standard Model predictions for semileptonic decays of heavy mesons containing a single heavy quark. At the quark level these decays proceed at first order in the weak coupling constant G_F^2. The decaying heavy quark interacts via the strong force with the light quark which is active in the decay, and both interact with the spectator. These quark-quark interactions include exchanges of infra-red gluons, for which the QCD perturbation expansion is inadequate; any renormalization condition results in a large value of the coupling, or in large logarithmic coefficients, either of which interdicts the perturbative approach.

Lattice QCD does not rely on formulating an asymptotic expansion in the QCD coupling. Instead the whole path integral (PI) is considered directly, so that matrix elements may be evaluated even when the strong coupling in some scheme is of O(1). The PI is expressed in terms of classical fields on a finite Euclidean spacetime lattice, and in terms of an action which becomes the Euclidean QCD

action in the continuum limit, with bare parameters chosen to make the lattice a practical size. The lattice spacing is extracted from the calculation of some mass or length scale.

The lattice PI used in this work is:

$$Z = \int \prod \mathrm{d}\mathcal{U}\mathrm{d}\bar{\psi}\mathrm{d}\psi \exp\left(-S[\mathcal{U},\bar{\psi},\psi]\right) \tag{2.1}$$

$$S[\mathcal{U},\bar{\psi},\psi] = S_{\text{gauge}}[\mathcal{U}] + S_{\text{quark}}[\mathcal{U},\bar{\psi},\psi] \tag{2.2}$$

$$S_{\text{gauge}} = \beta \sum_{\substack{U_x^{\mu\nu}\in \\ \text{plaquettes}}} \mathrm{Tr}\left(\mathbb{1}_3 - \frac{1}{2}(U_x^{\mu\nu} + U_x^{\mu\nu\dagger})\right) \tag{2.3}$$

$$S_{\text{quark}} = \bar{\psi}_x M_{xy}(\mathcal{U})\psi_y \tag{2.4}$$

$$M_{xy} = \frac{1}{2\kappa}\delta_{xy} + U_x^{\mu}(1_\mu + \gamma_\mu)\delta_{(x+\hat{\mu})y} + U_{(x-\hat{\mu})}^{\mu\dagger}(1_\mu - \gamma_\mu)\delta_{(x-\hat{\mu})y} + \left[\frac{i}{2}c_{\text{sw}}P_x^{\mu\nu}\sigma_{\mu\nu}.\delta_{xy}\right] \tag{2.5}$$

$$P_x^{\mu\nu} = U_x^{\mu\nu} + U_{x-\hat{\mu}}^{\mu\nu} + U_{x-\hat{\nu}}^{\mu\nu} + U_{x-\hat{\mu}-\hat{\nu}}^{\mu\nu} \tag{2.6}$$

U_x^μ is the colour gauge field related to the continuum gauge potential $A^\mu(x)$ by $U_x^\mu = \exp\left(ig\int_x^{x+\hat{\mu}} A^\mu \mathrm{d}x\right)$, and $U_x^{\mu\nu} = U_x^\mu U_{x+\hat{\mu}}^\nu U_{x+\hat{\mu}+\hat{\nu}}^{\mu\dagger} U_{x+\hat{\nu}}^{\nu\dagger}$ is the product of links around an elementary plaquette. The action S has the familiar (Euclidean) QCD action

$$\mathcal{S} = \int \mathrm{d}^4x \left(-\frac{1}{4}\mathrm{Tr}F^{\mu\nu}F_{\mu\nu}(x) + \overline{\psi}\left(\not{\partial} + ig\not{A}\right)\psi(x) + m\overline{\psi}\psi(x)\right) \tag{2.7}$$

as its continuum limit.

The pure gauge part of the lattice action has no discretization errors of O(a). The fermionic part of the action can be tuned to remove O(a) errors by adding the irrelevant operator $P^{\mu\nu}\sigma_{\mu\nu}$ with coefficient $\frac{i}{2}c_{\text{sw}}(\beta)$. The c_{sw} which remove O(a) discretization errors from the PCAC relation (Eq$^{\text{n}}$ 3.10) are calculated in Ref.[23],

given in terms of $g_0^2 = 6/\beta$:

$$c_{\rm sw} = \frac{1 - 0.656 g_0^2 - 0.152 g_0^4 - 0.054 g_0^6}{1 - 0.922 g_0^2} \tag{2.8}$$

yielding $c_{\rm sw}^{\beta=6.2} = 1.61$ and $c_{\rm sw}^{\beta=6.0} = 1.76$, for this work.

Integrating over the quark fields ψ, $\bar{\psi}$, the partition function simplifies to:

$$Z = \int \prod \mathrm{d}\mathcal{U} \det\left(M(\mathcal{U})\right) \exp\left(-S_{\rm gauge}[\mathcal{U}]\right) \tag{2.9}$$

The determinant $\det\left(M(\mathcal{U})\right)$ is moved through the integral sign, in what is known as the quenched approximation. This determinant then disappears completely from observables, which are ratios of the partition function and its moments. The quenched approximation can be shown to correspond to neglecting virtual quark loops [24].

Non-local effective operators $\hat{\Omega}_{\rm M}^{\dagger}$ and $\hat{\Omega}_{\rm M}$ with appropriate flavour and spin are manufactured for the creation and destruction of mesons. While a general operator with the correct symmetry properties may be relied on to overlap with the lattice states of interest, $\hat{\Omega}_{\rm M}^{\dagger}$ and $\hat{\Omega}_{\rm M}$ are constructed in order to enhance the overlap and increase the signal relative to the intrinsic variance of the Monte Carlo samples. The construction methods are described in Ref. [25] (for heavy-light mesons, based on a discretization of the appropriate Laguerre function) and in Ref. [26] (for light-light mesons, using an iterative method). The matrix element for semileptonic PS decay is then obtained from the expectation value of $\hat{\Omega}_{\rm M} J_W^{\mu} \hat{\Omega}_{\rm M}^{\dagger}$ in the partition function Z. The correlation function $\langle 0|\hat{\Omega}_{\rm M} J_W^{\mu} \hat{\Omega}_{\rm M}^{\dagger}|0\rangle$ is equal to the trace of propagators of the three quarks involved in the decay, interleaved with the gamma matrices encoding the Lorentz transformation properties of the meson and the current (Eq$^{\rm n}$ 2.13).

The quark propagators $G(x,y)$ are expectation values of quark bilinears $\bar{\psi}_y\psi_x$ in the partition function Z, which in the quenched approximation evaluate to:

$$G(x,y) = \frac{1}{Z}\int \prod \mathrm{d}\mathcal{U} M_{xy}^{-1}(\mathcal{U}) \exp\left(-S_{\mathrm{gauge}}[\mathcal{U}]\right) \tag{2.10}$$

where both G and M^{-1} have suppressed spin and colour indices. A set is created of $\mathcal{U}$ of $216_{\beta=6.2}$ $(305_{\beta=6.0})$ gauge configurations selected with probability measure

$$\mathrm{d}\Phi = \frac{1}{Z}\mathrm{d}\mathcal{U} \exp\left(-S_{\mathrm{gauge}}[\mathcal{U}]\right), \tag{2.11}$$

using a combination of Cabibbo-Marinari [27] and over-relaxed heat bath algorithm [28]. The average over the ensemble $\mathcal{U}$ of the components of M_{xy}^{-1} is a Monte-Carlo approximation to the integral $G(x,y)$:

$$G(x,y) \simeq \frac{1}{N}\sum_i M_{xy}^{-1}(\mathcal{U}_i) \tag{2.12}$$

The light meson operator $\hat{\Omega}_{\mathrm{M}}(0)$ is fixed at the origin in this work for logistical reasons. The heavy meson operator $\hat{\Omega}_{\mathrm{M}}^{\dagger}(x)$ is permitted to occupy any position in space, with its time coordinate fixed at $28a$. The spatial coordinate $\vec{x}$ is Fourier integrated immediately to create an 'extended propagator' (described in Ref. [29]), with great savings in storage requirements. The current operator $J^{\mu}(y)$ is permitted to occupy any site on the lattice. The final three-point correlation function for PS decay via the effective weak current J^{μ} is then given by the trace:

$$C_{3\mathrm{pt}}(0,x,y) = \mathrm{Tr}\Gamma^{\alpha}G(y,0)\Gamma^{\beta}G^{\dagger}(y,x)\Gamma^{\gamma}G^{\dagger}(x,0) \tag{2.13}$$

where the identity $G(s,r) = \Gamma_5 G^{\dagger}(r,s)\Gamma_5$ has been used, and each Γ represents any element of the algebra. Throughout this discussion, quark and meson flavours have been suppressed. A diagram of a typical process, containing conventional

names and symbols for the particles involved in the decay and their degrees of freedom, can be found in Fig. 2.1.

The coefficients of this correlator's Fourier series in the spatial variables $\vec{x}$ and $\vec{y}$ are projected out for discrete values of the respective conjugate labels $\vec{p}$ and $\vec{k}$ s.t. $|\vec{p}| \leq \pi/N_{\mathrm{xyz}}a$ and $|\vec{k}| \leq \pi/\sqrt{2}N_{\mathrm{xyz}}a$. The labels $\vec{p}$ ans $\vec{k}$ correspond to the spatial part of the momenta p and k in Fig. 2.1. At large times, the contribution to the correlator from the lowest states dominates all others, and the desired matrix element is extracted from a fit:

$$\tilde{C}^{\vec{p},\vec{k}}_{\mathrm{3pt}}(0 \ll t_x \ll t_y) \simeq \langle \mathrm{P}(\vec{p})|J^{\mu}|\mathrm{P},\mathrm{V}(\vec{k})\rangle \times$$
$$\frac{\langle 0|\hat{\Omega}_{\mathrm{P}}|P(\vec{p})\rangle\langle 0|\Omega^{\mathrm{P,V}}|\mathrm{P},\mathrm{V}(\vec{k})\rangle e^{-E_{\vec{p}}t_y}e^{-E_{\vec{k}}(t_x-t_y)}}{4M_{\mathrm{P}}M_{\mathrm{P,V}}} \tag{2.14}$$

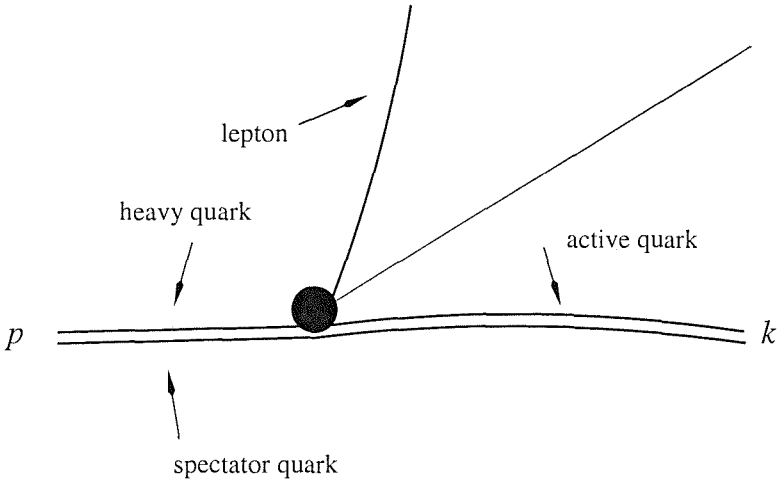

Figure 2.1: The objects in a semileptonic decay: Names and symbols used in this work. Time proceeds from left to right.

Two-point correlation functions for mesons are given by the trace of two quark

propagators:

$$C_{2\mathrm{pt}}(0,y) = \mathrm{Tr}\Gamma^a G(y,0)\Gamma^b G^\dagger(y,0) \tag{2.15}$$

where y can take values anywhere on the lattice. Inserting a complete set of states and translating the large-time operator to the temporal origin gives a function of y whose spatial fourier coefficients with labels $\vec{p}$ are the square overlap of the interpolation operators with the true lowest state, $|\langle 0|\hat{\Omega}_{\mathrm{P}}|\mathrm{P},\mathrm{V}(\vec{p})\rangle|^2$.

Extracting the three-point matrix element by translating the operators to the temporal origin requires knowledge of the lowest-state masses, which are fit directly from the two-point correlator in the large time region where the lowest state dominates:

$$\tilde{C}^{\vec{p}}_{2\mathrm{pt}}(0 \ll t) \sim \frac{Z^2}{2M}\left(e^{-E_{\vec{p}}t} \pm e^{-E_{\vec{p}}(T-t)}\right) \tag{2.16}$$

where the variable sign term originates from the finite size of the lattice, and depends on the behaviour of the interpolation operator under time reversal for periodic boundary conditions. The large time region is established by inspection for flatness of the quantity $\left(C_{2\mathrm{pt}}(0,t+1) - C_{2\mathrm{pt}}(0,t-1)\right)/C_{2\mathrm{pt}}(0,t)$ (twice sinh of the 'effective mass'). App. F shows an output set which is typical of this work.

Practical lattice simulations have access only to certain intermediate distance and momentum scales, and do not support the real processes D$\rightarrow \pi,\rho$ and B$\rightarrow \pi,\rho$. A guided extrapolation of matrix elements from around the D, K mass region is carried out to B and π, ρ masses. This extrapolation is broken down and described fully in Chap. 3.

Chapter 3

Extraction of Form Factors and Decay Constants

	Lattice I	Lattice II
β	6.2	6.0
Volume	$24^3 \times 48$	$16^3 \times 48$
N_{configs}	216	305
Heavy κ	$0.1200, 0.1233, 0.1266, 0.1299$	$0.1123, 0.1173, 0.1223, 0.1273$
Light κ	$0.1346, 0.1351, 0.1353$	$0.13344, 0.13417, 0.13455$
a^{-1} (GeV)	2.68(13)	2.12(18)
κ_{crit}	0.13581(2)	0.13525(2)
κ_{n}	0.13578(2)	0.13520(2)
κ_{s}	0.13495(2)	0.13476(4)

Table 3.1: Simulation parameters

The simulation parameters used in the work can be found in Tab. 3.1. This table includes the input values of quark mass and coupling and the number of lattice points, as well as the derived physical size of the lattice spacing and the hopping parameters κ_{critical}, κ_{normal} and κ_{str} corresponding to zero, 'normal' (a light-quark mass scale defined in Sec. 3.6) and strange quark masses respectively.

In order to make predictions for differential decay rates, form factors and decay constants, the lattice Green's function data must undergo a series of transformations. The processing of the lattice data breaks up into the following stages:

1. Implementing improvement of current operators to reduce artefacts from spacetime discretization
2. Extraction of meson masses, wavefunction factors and decay constants from two-point Green's functions
3. Matrix elements fit from three-point Green's functions
4. Transforming from Euclidean to Minkowski space
5. Extracting form factors from matrix elements
6. Changing the momentum transfer (q^2)
7. Changing the light mass
8. Changing the heavy mass
9. Extracting CKM elements, differential decay rates from form factors

These stages can in theory be performed in any order, ideally giving compatible answers (although masses and wavefunction factors are indispensable in the extraction of matrix elements from three-point functions, and the quark mass may only be improved after the light mass extrapolation when κ_{critical} has been determined). The order adopted in this work cuts down the total data storage required as much as possible at each stage. It has been suggested by Hashimoto [30] that in practice, due the inexactness of the various models, final predictions do indeed depend on the order in which the extrapolations are carried out. This suggestion is addressed in Chap. 7.

3.1 Improvement

O(a) improvement of the action has already been described in the previous chapter, and consists in adding the 'clover' term with coefficient $c_{\rm SW}$ determined in Ref. [23] (Tab. 3.2). Full O(a) improvement is also applied to the current operators, using the coefficients to O(a) are $Z_{\rm X}$, $b_{\rm X}$, $c_{\rm X}$ where $X \in \{\rm A, V\}$ according to the system:

$$V_\mu \rightarrow Z_{\rm V}\,(1 + b_{\rm V} a\overline{m}_{\rm q})\,(V_\mu + i c_{\rm V} a \partial_\nu T_{\mu\nu}) \tag{3.1}$$

$$A_\mu \rightarrow Z_{\rm A}\,(1 + b_{\rm A} a\overline{m}_{\rm q})\,(A_\mu + i c_{\rm A} a \partial_\mu P) \tag{3.2}$$

where the spinor parts of the pseudoscalar (P) and tensor ($T_{\mu\nu}$) flavour-changing currents are defined by $P = \overline{\psi}_a \gamma_5 \psi_b$ and $T = \overline{\psi}_a \sigma_{\mu\nu} \psi_b$, and $a\overline{m}_{\rm q}$ is the average mass of the two quark flavours a and b. The coefficients' values as determined by various authors are listed, with references, in Tab. 3.2. The bare mass of a quark is a function of the input hopping parameter κ which appears in the Lagrangian, and of $\kappa_{\rm critical}$:

$$am_{\rm q} = \frac{1}{2}\left(\frac{1}{\kappa_{\rm q}} - \frac{1}{\kappa_{\rm critical}}\right) \tag{3.3}$$

It is moreover useful to employ an improved definition of the quark mass, given by the following formula:

$$a\tilde{m}_{\rm q} = am_{\rm q}(1 + b_{\rm M} am_{\rm q}) \tag{3.4}$$

with $b_{\rm M}$ given in Tab. 3.2.

Almost all the improvement coefficients used in this work are calculated using non-perturbative (NP) methods. The most serious exception is the coefficient $c_{\rm V}$, whose only determination outside perturbation theory (Ref. [34]) predicts an

Coef-ficient		Favoured Value $\beta = 6.2$	Favoured Value $\beta = 6.0$		Included In Uncertainty $\beta = 6.2$	Included In Uncertainty $\beta = 6.0$
Z_V	Ref. [31]	0.7922	0.7809		–	–
Z_A	Ref. [31]	0.8067	0.7906		–	–
b_V	Ref. [31]	1.404	1.477		–	–
b_A	Ref. [32]	1.43	1.41	Ref. [33]	1.15	1.15
c_V	Ref. [33]	-1.58×10^{-2}	-1.63×10^{-2}	Ref. [34] Ref. [32]	-0.22 -2.58×10^{-2}	-0.32 -2.75×10^{-2}
c_A	Ref. [31]	-3.71×10^{-2}	-8.28×10^{-2}		–	–
b_M	Ref. [35]	-0.62	–	Ref. [33]	-0.6198	-0.6217

Table 3.2: Improvement coefficients used in this work

effect on matrix elements of up to 100% (to which the community has reacted skeptically [36]). The NP determination of the coefficient b_A gives a more heuristic cause for concern; improvement of the axial current using $b_A = 1.43_{\beta=6.2}, 1.41_{\beta=6.0}$ from Ref. [32] changes axial current matrix elements by a smaller but still uncomfortably large amount. In particular, the pseudoscalar decay constants on the two lattices are made to differ by up to 10% (*cf.* Tab. 6.1), which hardly constitutes improvement. To hedge, an alternative set of predictions for quantities involving the axial current is provided, using the previous best determined value of b_A from perturbation theory.

3.2 Masses, Wavefunction Factors and Decay Constants

The decay constants in the continuum theory of pseudoscalar and vector mesons, f_{P} and f_{V} are defined respectively as follows:

$$f_{\mathrm{P}} = \frac{\langle 0|A^{\mu}|\mathrm{P}(p)\rangle}{p^{\mu}} \tag{3.5}$$

$$f_{\mathrm{V}} = \frac{M_{\mathrm{V}}^{2}\xi_{r}^{\mu}}{\langle 0|V^{\mu}|\mathrm{V_r}(p)\rangle} \tag{3.6}$$

with μ a free index $\mu \in \{1 \ldots 4\}$, and ξ a pseudovector satisfying the polarization sum identity:

$$\sum_{r} \xi_{\mu r}(p)\xi_{\nu r}(p) = -g_{\mu\nu} + \frac{p_{\mu}p_{\nu}}{M_{\mathrm{V}}^{2}} \tag{3.7}$$

3.3 Matrix Elements from Three-point Green's functions

All information about matrix elements of current operators between states is contained in the three-point Green's functions G_{MJN}. The matrix element of the current operator J between the lowest states overlapping with M and N respectively can be extracted from behaviour of the three-point Green's function at times near a quarter the length of the lattice, which is both as far away as possible from the origin, where M is created, and from timeslice 28 out of 48, where N is created, in order to ensure that only ground states contribute. The asymmetric position of the extension point $t_x = 28$ helps to create a region in time which is free from the effects of unphysical time orderings. The exact region to be used for a given Green's function is chosen by inspection for flatness in

time after the theoretical time dependence has been divided out (for example, in the Green's function of Fig. 3.1, times 7-17 could be used). An estimate of the matrix element is obtained from each time coordinate in this supposed asymptotic region, and these estimates are subjected to a combined fit.

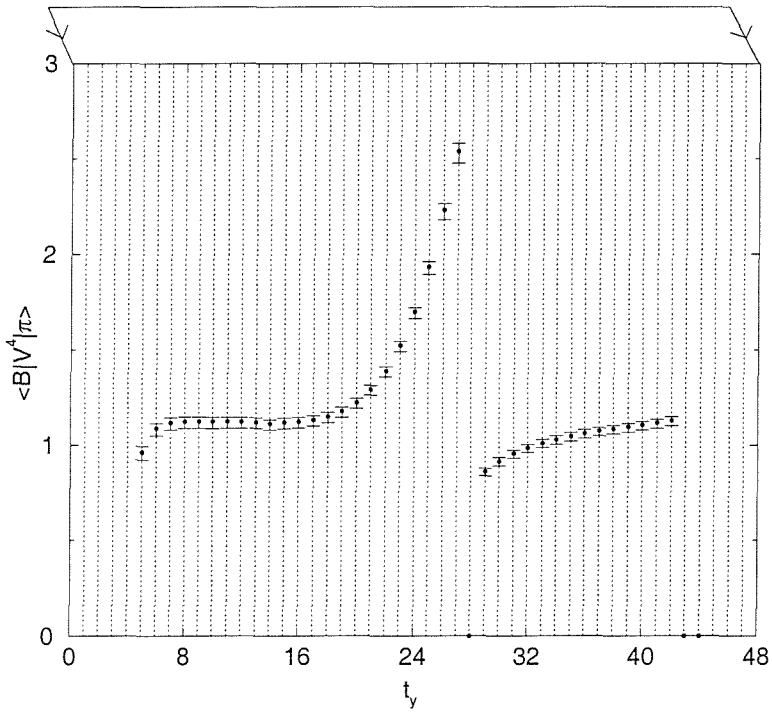

Figure 3.1: Estimate of matrix element of $\langle \mathrm{B}|V_4|\pi\rangle$ *vs.* time ($\kappa_{\mathrm{heavy}} = 0.12$, $\kappa_{\mathrm{light}} = 0.1346$, $\kappa_{\mathrm{spectator}} = 0.1346$, $\vec{p} = 0, \vec{k} = 0$, $\beta = 6.2$)

3.4 Minkowski from Euclidean

The Γ_μ matrices used in the lattice simulation, which obey anticommutation relations with a Euclidean Metric ($\{\Gamma_\mu, \mathrm{F}_\nu\} = \delta_{\mu\nu}$), differ from those in a Minkowski space representation where the form factors are defined (*cf.* App. C). This difference is introduced, in combination with the Wick rotation, in order to ensure that the Euclidean action S_{E} is a positive definite quantity, and a valid probability function for use in a Monte-Carlo algorithm. The matrix elements of

operators which are proportional to gamma-matrices are multiplied by the appropriate phase before the Minkowski-space form factor decomposition is applied according to the recipe in App. C.

3.5 Form Factors from Matrix Elements

Lorentz-invariant information about the dependence of a matrix element on the momenta and polarizations of its particle states is expressed as a sum of quantities which transform in the same representation as that matrix element, each multiplied by an scalar 'form factor'. Form factors in this work are listed below:

There are 2 form factors for a $\langle \mathrm{P}(p)|V^\mu|\mathrm{P}'(k)\rangle$ matrix element(f^+, f^0).

There is 1 form factor for a $\langle \mathrm{P}(p)|V^\mu|\mathrm{V}_r(k)\rangle$ matrix element(V).

There are 3 form factors for a $\langle \mathrm{P}(p)|A^\mu|\mathrm{V}_r(k)\rangle$ matrix element(A^2, A^1, A^0).

The relationship between the matrix elements and the form factors $f^+ \ldots A^0$ is given in App. B.

The number of form factors is equal to the number of matrix elements which cannot be related to one another by a connected Lorentz transformation. Matrix elements are calculated with all possible values of Lorentz indices. In addition states are given different momenta which are related by rotations. In this work the traditional approach is adopted, which is to average together matrix elements related by rotation, and to neglect those matrix elements which vanish theoretically (although they could in principle influence the fit through non-zero correlations with non-vanishing matrix elements). There are more matrix elements than form factors; minimization of the χ^2 statistic of the matrix elements gives a prescription for form factors (*cf.* App. A for details).

Models will be used later for the dependence of the form factors on q^2, M, m. Between them, the models for the form factors have a total of at least 10 unknown parameters which must be fit using simulation data. The use of these models is critical, to guide an extrapolation of a form factor when all three kinematic variables are changed from their values input in the lattice simulation, to those for decays of physical particles and at values of q^2 for which they can be measured. The lattice simulation is performed with 24 combinations of M and m, and 9 values of q^2 for each combination, in order to constrain the parameters in these models as much as possible. The total volume of form factor data at each value of the coupling therefore consists of 24 tables of the size of Tab. F.1.

3.6 Fixing the Parameters of the Theory

At this stage in the calculation the size of the lattice remains unknown, and the dimensionless parameters am_{normal}(q=u,d) and $am_{\text{spectator}}$ remain to be fixed. Lattice and numerical artefacts cause different definitions of physical parameters to produce mildly different results. In this work, the following order is adopted for defining the parameters:

1. The scale a is set from the gluonic observable r_0 [1]. $r_0(\beta)$ is calculated in [2]:

$$\ln\left(\frac{r_0}{a}\right) = 1.6805 + 1.7139(\beta - 6) - 0.8155(\beta - 6)^2 + 0.6667(\beta - 6)^3 \quad (3.8)$$

   Using $r_0 \simeq 0.49\text{fm} \simeq 2.5\,\text{GeV}^{-1}$ gives:

$$a^{\beta=6.2} = 0.13 r_0 = 0.33\,\text{GeV}^{-1} \qquad a^{\beta=6.0} = 0.19 r_0 = 0.48\,\text{GeV}^{-1} \quad (3.9)$$

2. The additive quark mass renormalization parameter, κ_{critical}, is set from the zero quark mass intercept of the best fit $a\tilde{m}_{\text{q}}(am_{\text{P}})$, using as a model the naive discretization of the PCAC relation in lowest order chiral perturbation theory:

$$a\tilde{m}_{\text{q}} \propto (am_{\text{P}})^2 \tag{3.10}$$

$a\tilde{m}_{\text{q}}$ is the arithmetic mean of the masses of the two quarks in the meson P_{q1q2}; $a\tilde{m}_{\text{q}} = \frac{1}{2}(a\tilde{m}_{\text{q1}} + a\tilde{m}_{\text{q2}})$.

3. The normal quark mass $m_{\text{normal}} = \frac{1}{2}(m_{\text{u}} + m_{\text{d}})$ is set from the pseudoscalar vector meson mass ratio $\frac{m_{\text{P}}}{m_{\text{V}}}$ as follows. First the ratio of the best fit functions from Eq$^{\text{ns}}$ 3.11 and 3.12 is constructed. Substituting the physical values of m_π and m_ρ then gives a quadratic equation for $\sqrt{m_{\text{q}}}$, the solution of which gives m_{normal}.

4. The strange quark mass m_{str} is set from the strange-normal pseudoscalar (K) mass. Starting from the best fit function for Eq$^{\text{n}}$ 3.11, the K mass is substituted for am_{P}, and the average $\frac{1}{2}(am_{\text{normal}} + am_{\text{str}})$ is substituted for am_{q}. The equation is rearranged and m_{str} is calculated.

Variations on this procedure are explored, to estimate the inconsistency of different parameter fixing schemes. The scale a is alternatively set from the pion decay constant f_π and the rho mass m_ρ. The strange quark mass is alternatively set from the mass of the strange-normal vector particle (K*) and from the strange-strange vector particle (assumed to correspond to the ϕ).

3.7 Changing the Momentum Transfer for Form Factors

The form factor may be calculated for any kinematically allowed ($0 < q^2 < q^2_{\mathrm{max}}$, $q^2_{\mathrm{max}} = M^2+m^2-2Mm$) value of the momentum transfer and still be a result with physical meaning, so it is not strictly necessary to extrapolate the form factor systematically to a different momentum transfer. However, a direct comparison with existing experimental results for $\mathrm{B} \to \pi \mathrm{l} \nu_{\mathrm{l}}$ requires a prediction in the region of reasonably small momentum transfer $q^2 \ll q^2_{\mathrm{max}}$. Furthermore, gaining a moderate ability to scale the form factors in q^2 at the outset allows a theoretically robust extrapolation in heavy mass (Sec. 3.9), for which, according to HQET, the base points should lie on a trajectory in q^2 of $v \cdot k = \mathrm{const.}$, with v the four-velocity of the heavy meson $v = \frac{1}{M}p$. (q^2 is related to $v \cdot k$ by $q^2 = M^2 + m^2 - 2Mv \cdot k$). This initial scaling entails an interpolation, which is a new addition to the fairly well established system used in previous calculations *e.g.* Ref. [37].

The favoured ansatz for interpolating all of the form factors in q^2 is a single pole model, chosen primarily for its simplicity and smoothness. Alternative smooth ansatz are used to construct a systematic error bar:

- a straight line
- a rational polynomial
- a pole of multiplicity 2.

3.8 Changing the Light Mass

The relation between light pseudoscalar mass am_{P} and quark mass $a\tilde{m}_{\mathrm{q}}$ follows directly from the partial conservation of axial current [38]:

$$a\tilde{m}_{\mathrm{q}} \sim X_{m_{\mathrm{p}},1}(am_{\mathrm{P}})^2 \tag{3.11}$$

The dependence of light decay constants and vector state masses, and of all heavy-light masses and decay constants, is assumed to be linear in the light quark mass:

$$am_{\mathrm{V}} \sim X_{m_{\mathrm{V}},0} + X_{m_{\mathrm{V}},1}(am_{\mathrm{P}})^2 \tag{3.12}$$

$$af_{\mathrm{P}} \sim X_{f_{\mathrm{P}},0} + X_{f_{\mathrm{P}},1}(am_{\mathrm{P}})^2 \tag{3.13}$$

$$af_{\mathrm{V}} \sim X_{f_{\mathrm{V}},0} + X_{f_{\mathrm{V}},1}(am_{\mathrm{P}})^2 \tag{3.14}$$

An ansatz for the fitting the dependence on the light pseudoscalar meson mass m_{P} of a heavy pseudoscalar to light pseudoscalar form factor $f_i(m_{\mathrm{heavy}}, q^2, m_{\mathrm{light}})$ must be accompanied by the specification of some trajectory in the other two variables, the momentum transfer q^2 and the heavy pseudoscalar mass M_{p}. In this work the constraint is $q^2 \sim$ const, $M_{\mathrm{p}} \sim$ const. The form factor is assumed to be an analytic function of the quark mass, which itself is an analytic function of the light pseudoscalar meson mass squared (from chiral perturbation theory, *cf.* Eq$^{\mathrm{n}}$ 3.11). The following ansatz arises from a power series expansion of the form factor in the squared pseudoscalar meson mass $(am_{\mathrm{P}})^2$, truncated at $\mathcal{O}((am_{\mathrm{P}})^2)$:

$$f(am_{\mathrm{P}}) \sim X_{f,0} + X_{f,1}(am_{\mathrm{P}})^2 \tag{3.15}$$

where $f \in \{f^+, f^0\}$.

The ansatz for the dependence of the pseudoscalar to vector form factors is linear

in the vector meson mass and is truncated at $\mathcal{O}(am_{\mathrm{V}})$:

$$f(am_{\mathrm{V}}) \sim X_{VA,0} + X_{VA,1} am_{\mathrm{V}} \tag{3.16}$$

where $f \in \{A^0, A^1, A^2, V\}$.

3.9 Changing the Heavy Mass

An analysis of the higher-dimensional operators contributing to heavy-light matrix elements in HQET (*cf.* Ref. [39]) prescribes the following forms for the scaling of decay constants and form factors at leading order in the heavy mass scale M near the heavy quark limit, and at fixed recoil variable $v \cdot k$:

$$f_P \sqrt{M} \Theta(M) \simeq const. \tag{3.17}$$

$$f_V M^{-\frac{3}{2}} / \Theta(M) \simeq const. \tag{3.18}$$

$$f_{\mathrm{I}} \sqrt{M} \Theta(M) \simeq const. \tag{3.19}$$

$$(f_{\mathrm{II}} / \sqrt{M}) \Theta(M) \simeq const. \tag{3.20}$$

with $f_{\mathrm{I}} \in \{f^0, A^0, A^1, V\}$, $f_{\mathrm{II}} \in \{f^+, A^2\}$, and M a scale associated with the heavy quark mass, usually taken to be some definition of the heavy quark mass itself in the literature. In this work M is the mass of that heavy meson appropriate to the quantity being extrapolated, *e.g.*, $M = M_{\mathrm{V}_s}$ for a strange vector decay constant. Θ is the leading order QCD radiative correction:

$$\Theta(M) = \left(\frac{\alpha_{\mathrm{s}}(M)}{\alpha_{\mathrm{s}}(M_B)} \right)^{2/11} \tag{3.21}$$

The constraint of constant $v \cdot k$ fixes the trajectory in q^2 for the form factors, with the light mass m_π, m_ρ *etc.* naturally chosen to be constant. Ansatz suitable

for a fit are prepared by including correction terms in $\frac{1}{M}$ and $\frac{1}{M^2}$:

$$f_{\rm P}\sqrt{M}\Theta(M) \sim X_{P,0} + \frac{X_{P,1}}{M} + \frac{X_{P,2}}{M^2} \quad (3.22)$$

$$f_{\rm V}M^{-\frac{3}{2}}/\Theta(M) \sim X_{P,0} + \frac{X_{P,1}}{M} + \frac{X_{P,2}}{M^2} \quad (3.23)$$

$$f_{\rm I}\sqrt{M}\Theta(M) \sim X_{I,0} + \frac{X_{I,1}}{M} + \frac{X_{I,2}}{M^2} \quad (3.24)$$

$$(f_{\rm II}/\sqrt{M})\Theta(M) \sim X_{II,0} + \frac{X_{II,1}}{M} + \frac{X_{II,2}}{M^2} \quad (3.25)$$

The 4 base points for the form factor fit have been prepared so as to lie on the constant $m, v\cdot k$ trajectory *cf.* Sec. 3.7. Each form factor and decay constant is now calculable at the masses of physical particles. The process is complete.

3.10 CKM Elements and Decay Rates from Form Factors

In the limit of zero lepton mass, the decay rates for the semileptonic decays *e.g.* for the B meson into a single species of massless lepton $\mathrm{B}\to\pi\mathrm{l}\nu_{\mathrm{l}}$ and $\mathrm{B}\to\rho\mathrm{l}\nu_{\mathrm{l}}$ are given by the following formulae: [40]:

$$\Gamma_{\mathrm{B}\to\pi} = \frac{|V_{\rm ub}|^2 G_{\rm F}^2}{192\pi^3 m_{\rm B}^3}\int_0^{q^2_{\rm max}} |f^+(q^2)|^2 \times \lambda_\pi(q^2)^{\frac{3}{2}}\mathrm{d}q^2 \quad (3.26)$$

$$\Gamma_{\mathrm{B}\to\rho} = \frac{|V_{\rm ub}|^2 G_{\rm F}^2}{192\pi^3 m_{\rm B}^3}\int_0^{q^2_{\rm max}} \mu(q^2) \times q^2 \times \lambda_\rho(q^2)^{\frac{1}{2}}\mathrm{d}q^2 \quad (3.27)$$

$$\lambda_{\rm x}(q^2) = (m_{\rm B}^2 + m_{\rm x}^2 - q^2)^2 - 4m_{\rm B}^2 m_{\rm x}^2 \quad (3.28)$$

$$\mu(q^2) = \frac{1}{q^2}\left(\frac{2m_{\rm B}^2|\vec{p}|^2}{(m_{\rm B}+m_\rho)m_\rho}A^{(2)}(q^2) - \frac{\left(m_{\rm B}^2 - m_\rho^2 - q^2\right)(m_{\rm B}+m_\rho)}{2m_\rho}A^1(q^2)\right)^2 +$$
$$\left((m_{\rm B}+m_\rho)\,A^1(q^2) + \frac{2m_{\rm B}|\vec{p}|}{m_{\rm B}+m_\rho}V(q^2)\right)^2 +$$

$$\left((m_{\mathrm{B}} + m_\rho)\, A^1(q^2) - \frac{2m_{\mathrm{B}}|\vec{p}|}{m_{\mathrm{B}} + m_\rho} V(q^2) \right)^2 \tag{3.29}$$

$$|\vec{p}| = \left(\left(\frac{q^2 - m_{\mathrm{B}}^2 - m_\rho^2}{2m_{\mathrm{B}}} \right)^2 - m_\rho^2 \right)^{\frac{1}{2}} = \left(\frac{\lambda_\rho(q^2)}{4m_{\mathrm{B}}^2} \right)^{\frac{1}{2}} \tag{3.30}$$

Analogous formulae apply for the D decays $\mathrm{D} \to \mathrm{Kl}\nu_\mathrm{l}$, $\mathrm{D} \to \pi \mathrm{l}\nu_\mathrm{l}$ and $\mathrm{D} \to \mathrm{K^*l}\nu_\mathrm{l}$, $\mathrm{D} \to \rho \mathrm{l}\nu_\mathrm{l}$ with the modifications $|V_{\mathrm{ub}}| \to |V_{\mathrm{cs}}|$, $|V_{\mathrm{cd}}|$, $m_{\mathrm{B}} \to m_{\mathrm{D}}$ and $m_\pi \to m_{\mathrm{K}}$, $m_\rho \to m_{\mathrm{K^*}}$ as appropriate. That zero lepton mass is a robust approximation can be inferred from Ref. [41]. It is now possible to give predictions using *e.g.* the world average value of $|V_{\mathrm{ub}}|$ for the $\mathrm{B} \to \rho \mathrm{l}\nu_\mathrm{l}$ differential decay rate, which can be compared directly to an imprecise measurement in large bins from CLEO [5]. Comparisons can also be made for the differential decay rates in the better known $\mathrm{D} \to \mathrm{Kl}\nu_\mathrm{l}$ and $\mathrm{D} \to \mathrm{K^*l}\nu_\mathrm{l}$ cases. The differential decay rate results are the first to be presented in Chap. 4.

A couple of functions are now used to model the dependence of a form factor on q^2. One is the pole dominance set:

$$f^{\mathrm{I}} \sim \frac{X_0}{1 - X_1 q^2} \tag{3.31}$$

$$f^{\mathrm{II}} \sim \frac{X_0}{(1 - X_1 q^2)^2} \tag{3.32}$$

Although f^0 and A^0 do not appear explicitly in the expression for the decay rate, they contain information about their partners through the constraints of the parameterization

$$f^0(0) = f^+(0) \tag{3.33}$$

$$A^0(0) = \frac{m_{\mathrm{P}} + m_{\mathrm{V}}}{2m_{\mathrm{V}}} A^1(0) - \frac{m_{\mathrm{P}} - m_{\mathrm{V}}}{2m_{\mathrm{V}}} A^2(0) \tag{3.34}$$

which appear after the matrix elements are asserted to be non-singular at $q^2 = 0$. Enforcing the constraint on the axial form factors is not practical and so, in this

work, A^0 is truly irrelevant.

The pole dominance perspective is that form factors may be largely influenced near $q^2_{\rm max}$ by a pole at the nearest resonance, which for f^+ is the $J^P = 1^-$ (vector) resonance with the appropriate flavour. The position of this resonance is known in the $B \to \pi l \nu_l$ (m_{B^*}=5324.9(18)MeV) and the $D \to \pi l \nu_l$ ($m_{D^{*0}}$=2006.7(5)MeV) cases. Becirevic and Kaidalov [7] thus propose the following (BK) parameterization for $f^+(q^2)$, $f^0(q^2)$, *e. g.* for $B \to \pi l \nu_l$ (the relative numbers of poles are prescribed by HQET, and are simply consequence of demanding consistency with Eq$^{\rm ns}$ 3.22–3.25):

$$f^+(q^2) \sim \frac{c_B(1-\alpha)}{(1-\frac{q^2}{m^2_{B^*}})(1-\frac{\alpha q^2}{m^2_{B^*}})} \tag{3.35}$$

$$f^0(q^2) \sim \frac{c_B(1-\alpha)}{1-\frac{q^2}{\beta m^2_{B^*}}} \tag{3.36}$$

Form factors for decays to a vector final state are also modeled as poles. However, although the principle of pole dominance is widely used in an exploratory context, it is rarely clear *a priori* just how important the non-analytic structure of the form factors beyond this pole will be. For this reason, the position of the leading poles in the $P \to V l \nu_l$ form factors are treated as free parameters in the fit even where they are approximately known:

$$V(q^2) \sim \frac{V_0}{(1-\frac{q^2}{m^2_V})^2} \tag{3.37}$$

$$A^{(2)}(q^2) \sim \frac{A^{(2)}_0}{(1-\frac{q^2}{m^2_{A^{(2)}}})^2} \tag{3.38}$$

$$A^1(q^2) \sim \frac{A^1_0}{1-\frac{q^2}{m^2_{A^1}}} \tag{3.39}$$

$$A^0(q^2) \sim \frac{A^0_0}{(1-\frac{q^2}{m^2_{A^0}})^2} \tag{3.40}$$

Again, the relative multiplicities of the poles are suggested by HQET. $m_{A^1} = m_{A^{(2)}}$ is imposed, since $A^{(2)}$ is noisy (*cf.* Figs. 4.3, 4.8, 4.13).

The relationship between the fitted pole positions and measured resonances with the appropriate quantum numbers is detailed in Secs. 4.1.1– 4.1.3.

With the help of these models, and after a numerical integration over q^2, $|V_{\mathrm{ub}}|$, $|V_{\mathrm{cs}}|$ and $|V_{\mathrm{cd}}|$ can be extracted.

Chapter 4

Results for Semileptonic Decay Rates and CKM Parameters

Results are presented to two significant figures. Where a result is referred to without quoting a value of β, $\beta = 6.2$ may be assumed, which is the closest to the continuum limit in this work. Where a number is quoted without error, the error is zero at the precision to which the number is given.

Preliminary results for P$\rightarrow$P differential decay rates, which could have been found in Ref. [42], are superceded by those of the following sections. The results of this chapter are shortly to be sumbitted for publication, and drafts are available on request from the author ([43, 44]).

q^2(GeV^2)	0.77	0.91	1.0	1.2	1.3
$f^+(q^2)$	1.0(3)	1.1(4)	1.1(4)	1.2(4)	1.3(5)
$f^0(q^2)$	0.87(3)	0.90(2)	0.92(2)	0.95(2)	0.98(3)
$\|V_{cs}\|^{-2}$dΓ/dq^2(ps^{-1}GeV^{-2})	0.065(5)	0.057(4)	0.049(4)	0.041(4)	0.033(3)

Table 4.1: Form factors and differential decay rate for D $\to$ Klν_l as functions of q^2, $\beta = 6.2$

4.1 Form Factors and Differential Decay Rates

4.1.1 D $\to$ Klν_l, D $\to$ K*lν_l

Form factors for physical D and K mesons are presented in Fig. 4.1, in which error bars contain statistical errors only. The differential decay rate in units of $|V_{cs}|^2$, extracted from Eq^n 3.26, is summarized in Tab. 4.1, which shows 5 representative values of q^2. The full set of data points and the best fit curve are depicted in figure Fig. 4.2.

The value obtained with $\beta = 6.2$ for $f_{D\to K}(0) = 0.7(2)$ is in good agreement with the average experimental determination $f_{D\to K}(0) = 0.71(3)(3)$ [8]. This agreement may suggest that quenching errors are moderate compared to the systematic errors introduced in the mass mutation procedure required for D$\to \pi$ and B$\to \pi$. The second effective pole in $f^+(q^2)$ is placed at a mass of 3.2(5)GeV, and the pole in f^0 at 2.4(2)GeV; the pole positions are reported for interest's sake and are not presented as spectroscopic predictions.

Form factors for D $\to$ K*lν_l are presented in sets of two, A^1, A^2(Fig. 4.3), followed by A^0, V(Fig. 4.4). The differential decay rate in units of $|V_{cs}|^2$ is summarized in Tab. 4.2, and depicted in full in figure Fig. 4.5. The pole in A^0 corresponds to a resonance of mass 2.5 GeV (*cf.* m_{D_s}=1968.5(6)MeV).

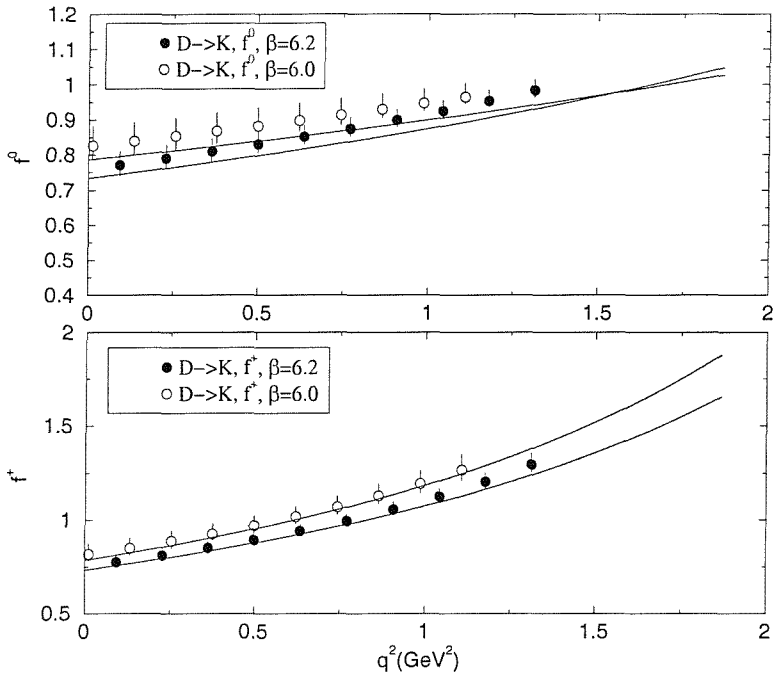

Figure 4.1: The form factors for D $\to$ K semileptonic decay ($\beta = 6.2$, $\beta = 6.0$)

q^2(GeV^2)	-0.012	0.072	0.16	0.24	0.33
$V(q^2)$	0.77(5)	0.78(5)	0.80(6)	0.81(6)	0.82(6)
$A^2(q^2)$	0.68(11)	0.70(13)	0.72(14)	0.74(16)	0.77(17)
$A^1(q^2)$	0.68(3)	0.68(3)	0.69(3)	0.70(3)	0.70(3)
$A^0(q^2)$	0.60(4)	0.62(4)	0.65(5)	0.67(5)	0.70(6)
$\lvert V_{cs}\rvert^{-2}$dΓ/dq^2(ps^{-1}GeV^{-2})	0.046(5)	0.053(4)	0.060(4)	0.066(4)	0.070(3)

Table 4.2: Form factors and differential decay rate for D $\to$ K*lν_l as functions of q^2, $\beta = 6.2$

4.1.2 D $\to \pi$lν_l, D $\to \rho$lν_l

D $\to \pi$ form factors are presented in Fig. 4.6. The differential decay rates are summarized in Tab. 4.3 and depicted in full in Fig. 4.6. The second effective pole in $f^+(q^2)$ is placed at a mass of 3.1(5)GeV, and the pole in f^0 at 2.5(3)GeV.

D $\to \rho$ form factors are presented in Figs. 4.8 and 4.9. The differential decay rates are summarized in Tab. 4.4 and depicted in full in Fig. 4.10. The

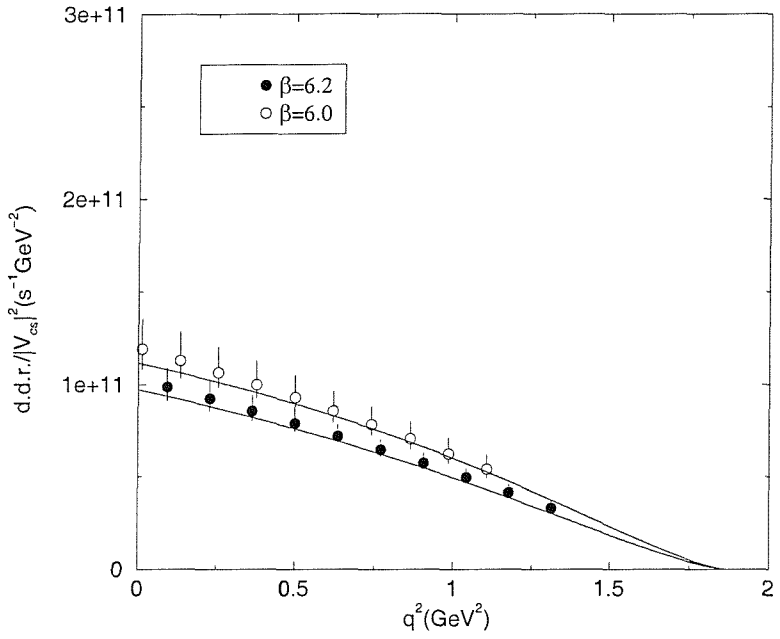

Figure 4.2: The differential decay rate for D $\to$ K semileptonic decay ($\beta = 6.2$, $\beta = 6.0$)

q^2(GeV^2)	0.72	0.86	1.0	1.1	1.3
$f^+(q^2)$	0.95(5)	1.0(5)	1.1(5)	1.1(6)	1.2(6)
$f^0(q^2)$	0.83(4)	0.85(4)	0.87(3)	0.90(3)	0.92(3)
$\|V_{cd}\|^{-2}d\Gamma/dq^2$(ps^{-1}GeV^{-2})	0.098(10)	0.094(9)	0.090(8)	0.086(8)	0.082(8)

Table 4.3: Form factors and differential decay rate for D $\to \pi l \nu_l$ as functions of q^2, $\beta = 6.2$

pole in A^0 is not well determined, but is consistent with a resonance of mass m_D ~1.9MeV. The pole in A^1, A^2 corresponds to a resonance of mass 2.4(4)MeV (*cf.* $m_{D_1^0}$=2422.2(18)MeV). The pole in V corresponds to a resonance of mass 2.3GeV, to be compared with $m_{D^{*0}}$=2006.7(5)MeV.

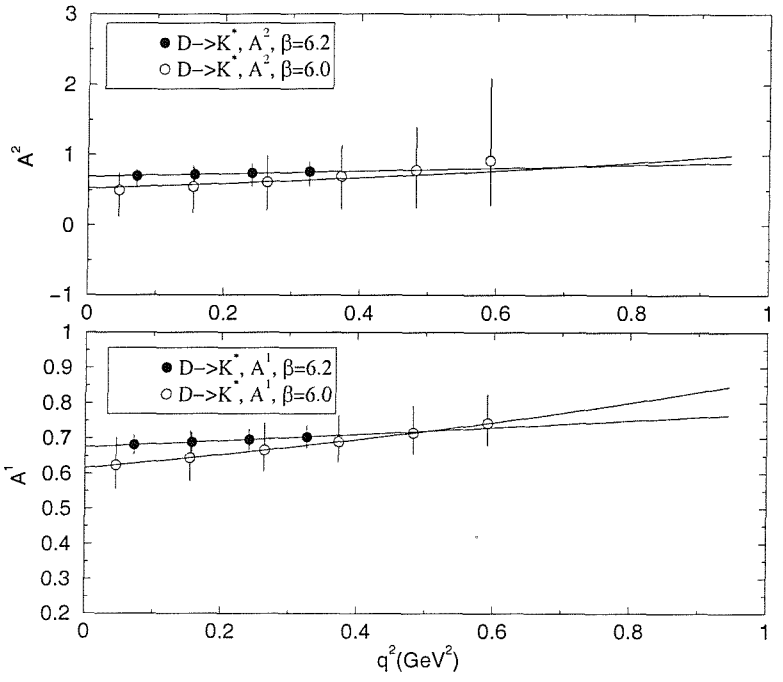

Figure 4.3: The form factors A^1, A^2 for D $\to$ K* semileptonic decay ($\beta = 6.2$, $\beta = 6.0$)

q^2(GeV^2)	-0.049	0.035	0.12	0.20	0.29
$V(q^2)$	0.68(5)	0.70(5)	0.71(6)	0.72(6)	0.73(7)
$A^2(q^2)$	0.60(12)	0.61(14)	0.63(16)	0.66(18)	0.68(20)
$A^1(q^2)$	0.62(3)	0.62(3)	0.63(3)	0.63(3)	0.64(4)
$A^0(q^2)$	0.56(5)	0.58(6)	0.60(6)	0.62(6)	0.64(7)
$\lvert V_{cd}\rvert^{-2}$dΓ/dq^2(ps^{-1}GeV^{-2})	0.047(13)	0.054(13)	0.059(13)	0.064(13)	0.068(13)

Table 4.4: Form factors and differential decay rate for D $\to \rho l\nu_l$ as functions of q^2, $\beta = 6.2$

4.1.3 B $\to \pi l\nu_l$, B $\to \rho l\nu_l$

The form factors f^+ and f^0 for the decay B $\to \pi l\nu_l$ are presented in Fig. 4.11. The quantities dΓ/d$q^2/|V_{ub}|^2$ and $\Gamma_{B\to\pi l\nu_l}/|V_{ub}|^2$ are summarized in Tab. 4.5 and depicted in full in Fig. 4.12, where the extrapolation to heavy mass includes $O\left(\frac{1}{M^2}\right)$ terms (*cf.* Eq^n 3.24). The second effective pole in $f^+(q^2)$ is placed at a mass of 9(2)GeV, and the pole in f^0 at 6.5(5)GeV. The y-axis scale of Fig. 4.12

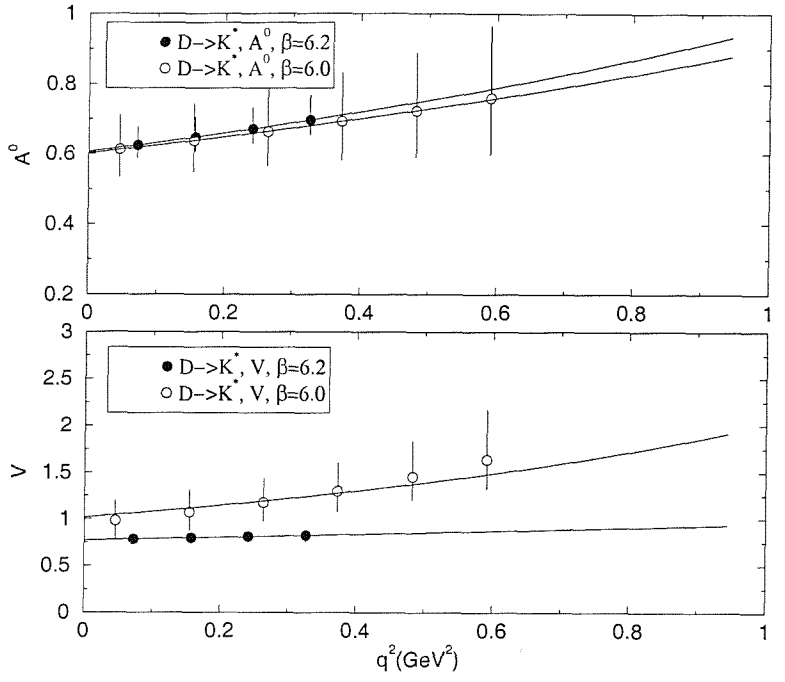

Figure 4.4: The form factors V, A^0 for D $\rightarrow$ K* semileptonic decay ($\beta = 6.2$, $\beta = 6.0$)

relative to Fig. 4.11 may make errors appear larger than expected.

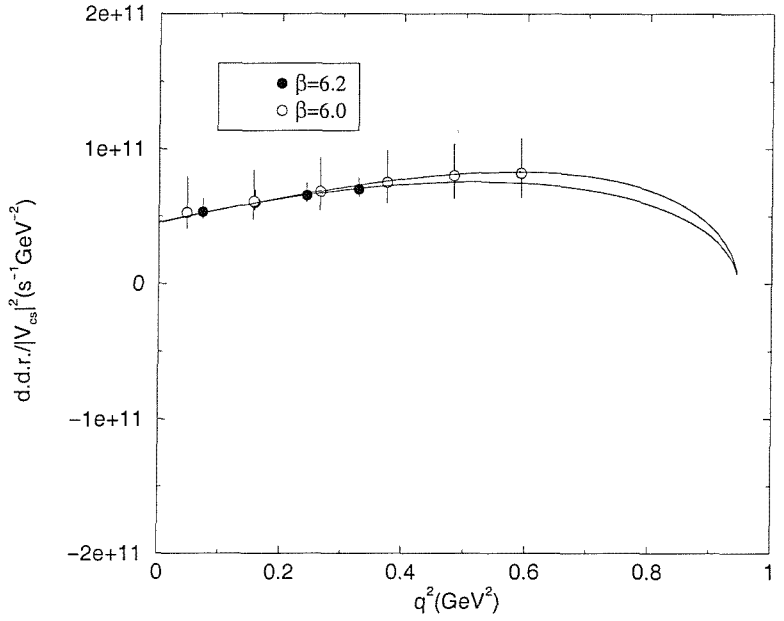

Figure 4.5: The differential decay rate for D $\rightarrow$ K* semileptonic decay ($\beta = 6.2$, $\beta = 6.0$)

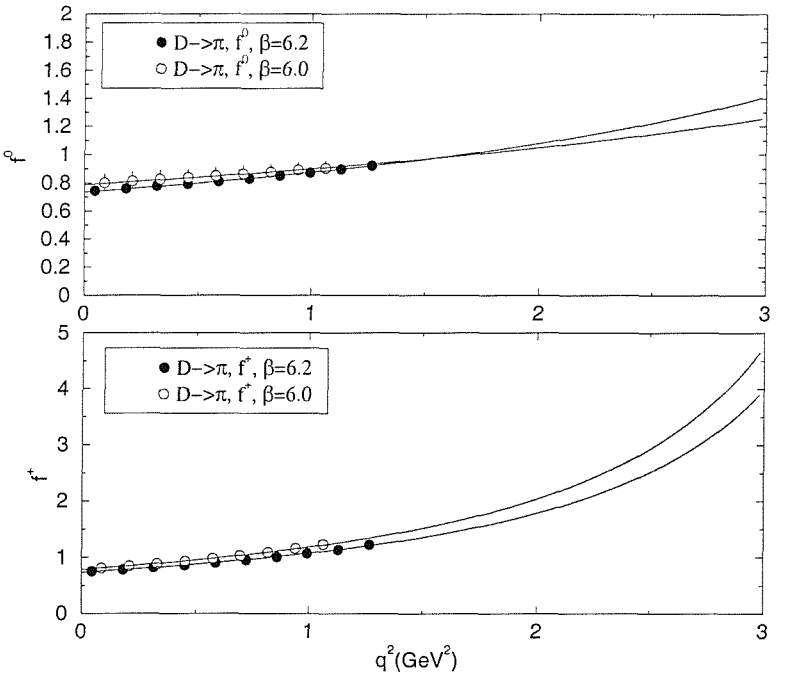

Figure 4.6: The form factors for D $\rightarrow \pi$ semileptonic decay ($\beta = 6.2$, $\beta = 6.0$)

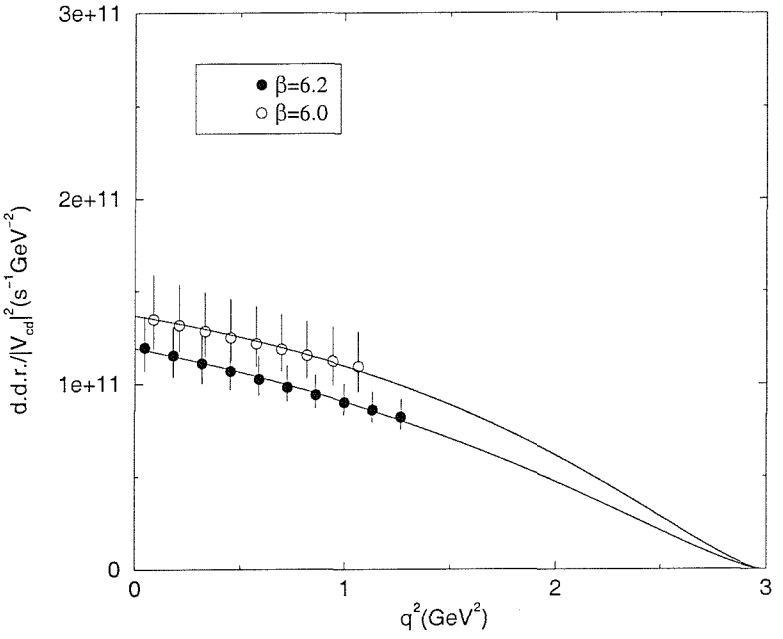

Figure 4.7: The differential decay rate for D $\rightarrow \pi$ semileptonic decay ($\beta = 6.2$, $\beta = 6.0$)

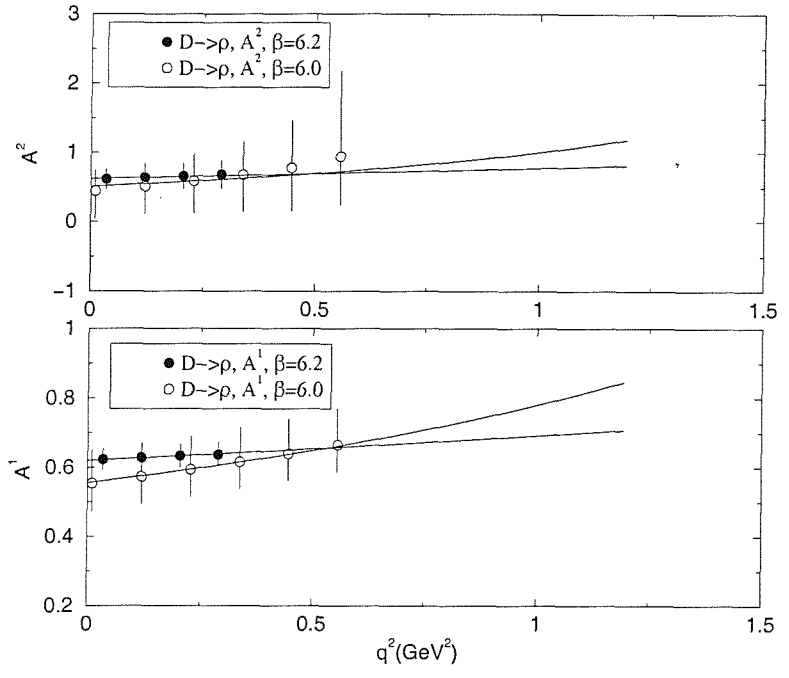

Figure 4.8: The form factors A^1, A^2 for D $\to$ ρ semileptonic decay ($\beta = 6.2$, $\beta = 6.0$)

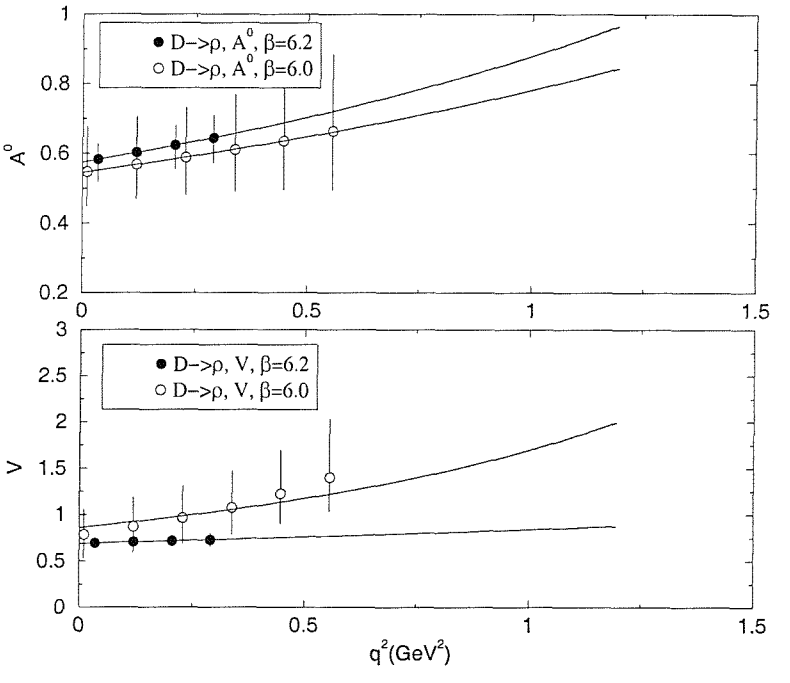

Figure 4.9: The form factors V, A^0 for D $\to$ ρ semileptonic decay ($\beta = 6.2$, $\beta = 6.0$)

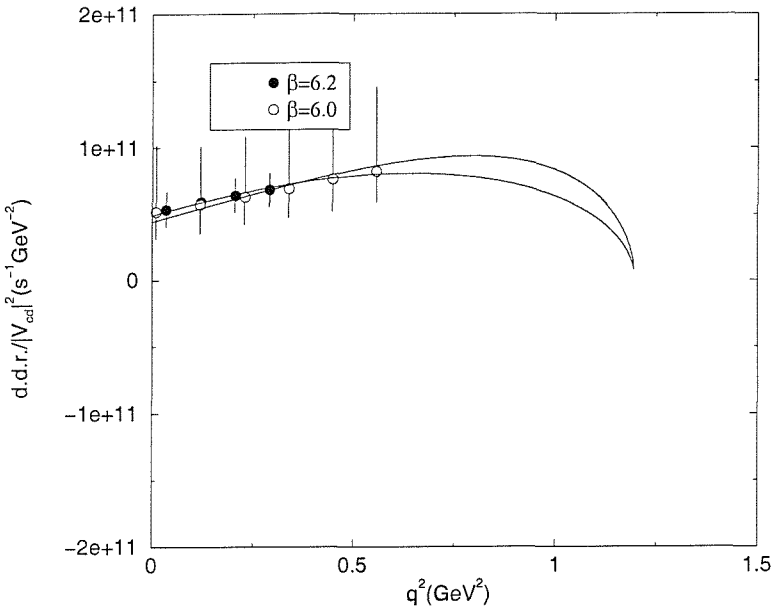

Figure 4.10: The differential decay rate for D $\rightarrow \rho$ semileptonic decay ($\beta = 6.2$, $\beta = 6.0$)

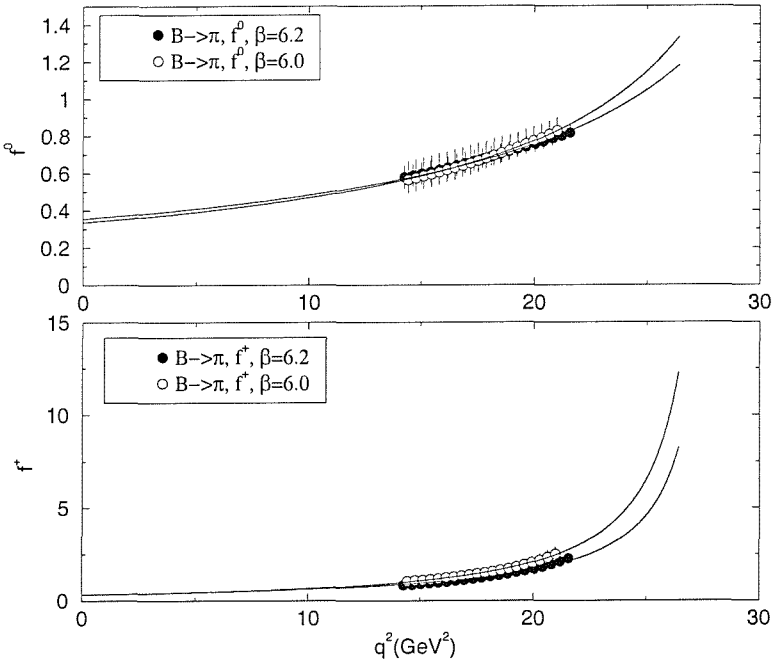

Figure 4.11: The form factors for B $\rightarrow \pi$ semileptonic decay ($\beta = 6.2$, $\beta = 6.0$)

$q^2(\,\mathrm{GeV}^2)$	20.0	20.4	20.8	21.2	21.6
$f^+(q^2)$	1.7(2)	1.8(2)	1.9(2)	2.1(2)	2.3(3)
$f^0(q^2)$	0.76(4)	0.77(4)	0.79(4)	0.80(4)	0.82(4)
$\|V_{\mathrm{ub}}\|^{-2}\mathrm{d}\Gamma/\mathrm{d}q^2(\mathrm{ps}^{-1}\mathrm{GeV}^{-2})$	0.32(7)	0.31(7)	0.30(7)	0.29(7)	0.29(7)

Table 4.5: Form factors and differential decay rate for $\mathrm{B} \to \pi \mathrm{l} \nu_{\mathrm{l}}$ as functions of q^2, $\beta = 6.2$

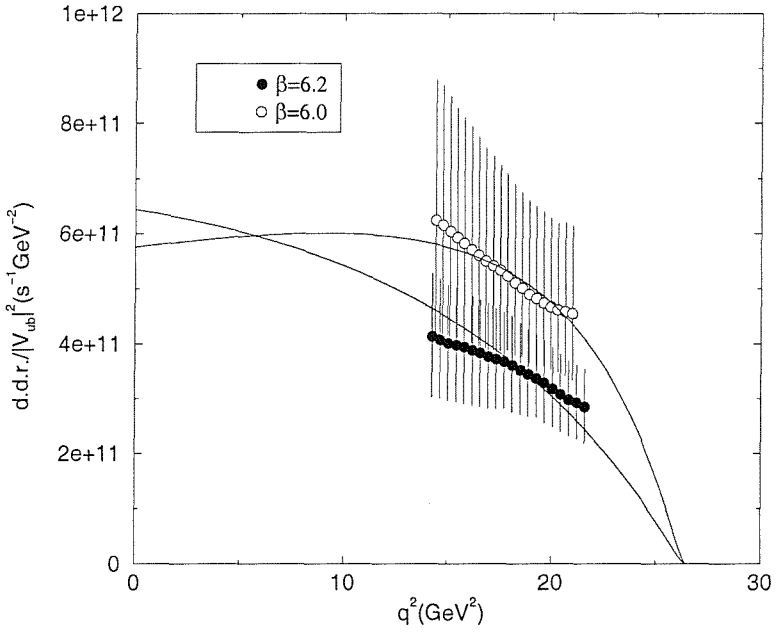

Figure 4.12: The differential decay rate for $\mathrm{B} \to \pi$ semileptonic decay ($\beta = 6.2$, $\beta = 6.0$)

$\mathrm{B} \to \rho$ form factors are presented in Figs. 4.13 and 4.14. The differential decay rates are summarized in Tab. 4.6 and depicted in full in Fig. 4.15. The pole in A^0 is not well determined, but is consistent with a resonance of mass m_{D} ~1.9MeV. The pole in A^0 corresponds to a mass of 5.6(9)GeV, and the poles in A^1 and V seem to center around a similar region. Experimental B spectroscopy is in its infancy, but a promising resonance peak known as the B_J has been found near 5700 MeV [45]. A set of quantum numbers has not yet been assigned, and HQET

$q^2(\,\mathrm{GeV}^2)$	16.6	16.9	17.1	17.3	17.6
$V(q^2)$	1.3(2)	1.3(2)	1.3(2)	1.2(3)	1.2(3)
$A^2(q^2)$	1.8(7)	1.9(8)	2.0(10)	2.1(12)	2.2(15)
$A^1(q^2)$	0.59(4)	0.59(5)	0.59(5)	0.59(5)	0.59(6)
$A^0(q^2)$	1.6(6)	1.7(6)	1.7(6)	1.8(6)	1.9(7)
$\|V_{\mathrm{ub}}\|^{-2}\mathrm{d}\Gamma/\mathrm{d}q^2(\mathrm{ps}^{-1}\mathrm{GeV}^{-2})$	1.3(2)	1.2(2)	1.2(2)	1.1(2)	1.1(2)

Table 4.6: Form factors and differential decay rate for $\mathrm{B} \to \rho l \nu_l$ as functions of q^2, $\beta = 6.2$

analysis suggests that the B_J may contain several resonances.

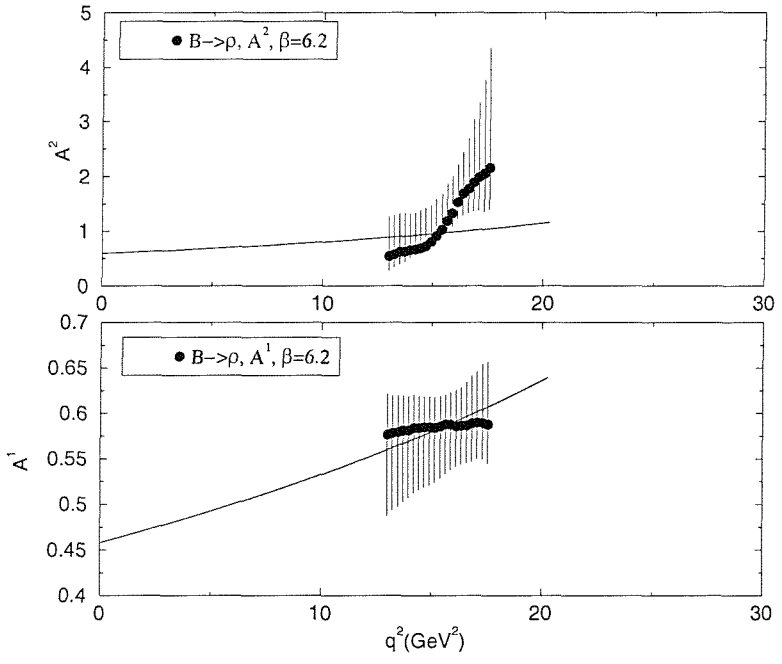

Figure 4.13: The form factors A^1, A^2 for $\mathrm{B} \to \rho$ semileptonic decay ($\beta = 6.2$)

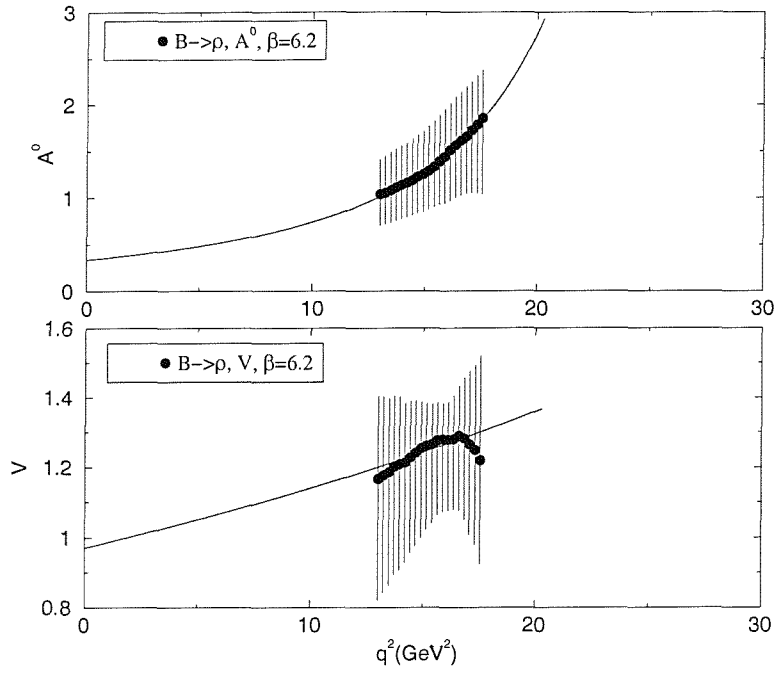

Figure 4.14: The form factors V, A^0 for B $\to \rho$ semileptonic decay ($\beta = 6.2$)

4.2 Integrated and Partially Integrated Decay Rates

4.2.1 Results

For massless leptons, the semileptonic heavy to light decay rate (*cf.* Eq$^{\text{n}}$ 3.27) is integrated using Simpson's rule with 500 strips, giving integrated decay rates of $\Gamma_{D\to Kl\nu_l}=1(0.07)\times10^{11}\ |V_{cs}|^2\ s^{-1}$, $\Gamma_{D\to\pi l\nu_l}=2(0.2)\times10^{11}\ |V_{cd}|^2\ s^{-1}$, $\Gamma_{B\to\pi l\nu_l}=1.1(0.3)\times 10^{13}\ |V_{ub}|^2\ s^{-1}$, $\Gamma_{D\to K^* l\nu_l}=5.9(0.5)\times10^{10}\ |V_{cs}|^2\ s^{-1}$, $\Gamma_{D\to\rho l\nu_l}=8(0.9)\times10^{10}\ |V_{cd}|^2\ s^{-1}$ and $\Gamma_{B\to\rho l\nu_l}=3.1(1.5)\times10^{13}\ |V_{ub}|^2\ s^{-1}$. Using lifetime and branching ratio data (*cf.* Tab. D.1, App.D) CKM moduli can be calculated directly, and are found to have the following values:

$$|V_{cs}|_{\beta=6.2} \quad = \quad 0.93(3)(10) \tag{4.1}$$

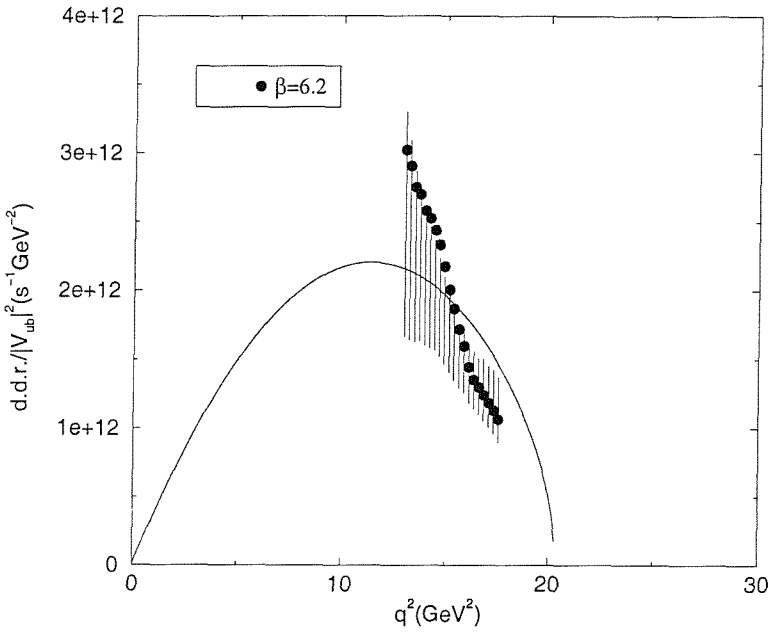

Figure 4.15: The differential decay rate for B $\rightarrow \rho$ semileptonic decay ($\beta = 6.2$)

$$|V_{\rm cd}|_{\beta=6.2} = 0.19(2)(7) \tag{4.2}$$

$$|V_{\rm ub}|_{\beta=6.2} = 3.2(4)(10) \times 10^{-3} \tag{4.3}$$

$$|V_{\rm cs}|_{\beta=6.0} = 0.86(3)(10) \tag{4.4}$$

$$|V_{\rm cd}|_{\beta=6.0} = 0.18(1)(7) \tag{4.5}$$

$$|V_{\rm ub}|_{\beta=6.0} = 3.0(5)(10) \times 10^{-3} \tag{4.6}$$

The world average values are [3]:

$$|V_{\rm cs}| = 0.975(1) \tag{4.7}$$

$$|V_{cd}| = 0.21(1) \tag{4.8}$$

$$|V_{\rm ub}| = 3.5(15) \times 10^{-3} \tag{4.9}$$

	$0 < q^2(\text{GeV}^2) < 7$	$7 < q^2(\text{GeV}^2) < 14$	$14 < q^2(\text{GeV}^2) < 20.3$
CLEO collab. [5]	7.6(44)	4.8(31)	7.1(31)
This work	7.4(13)	15(4)	10(1)

Table 4.7: Partially integrated rates from CLEO and this work for $B \to \rho l \nu_l$ over three bins, each covering approximately one third of the allowed range in q^2

(4.10)

The estimates at $\beta = 6.2$ of $|V_{cs}|$, $|V_{cd}|$ and $|V_{ub}|$ are found to be in comfortable accord with experiment. That the estimate at $\beta = 6.0$ for $|V_{cs}|$ is somewhat different from the world average, is attributed to lattice artefacts.

Although the error bars on both experimental and lattice calculations are large, the fact of agreement in all cases is heuristically supportive of the standard model. Scaling between the two values of β is variable, with violations between $\beta = 6.2$ and $\beta = 6.0$ results ranging from very small in the case of the $D \to Kl\nu_l$ differential decay rate, to up to 25% in the case of some of the less well-determined form factors for $B \to \rho l \nu_l$. In all cases, however, the scaling violation is less than the Monte-Carlo error, from which one may argue that little would be gained from having simulated using larger β.

Ref. [5] gives the total rate for $B \to \rho l \nu_l$ measured over three ranges of q^2, shown in Tab. 4.7 along with the corresponding estimate from this work.

4.2.2 Discussion

The reduction in statistical error relative to Ref. [37] is believed to be a side effect of extrapolating the form factors at constant q^2, and in particular, of interpolating the lattice form factors when choosing q^2 for the chiral extrapolation. The

	c_B	α	β	$f(0)$
$D \to Kl\nu_l$	0.58(8)	0.39(12)	1.3(2)	0.36(6)
$D \to \pi l\nu_l$	1.2(2)	0.37(13)	1.6(3)	0.73(0)
$B \to \pi l\nu_l$	1.1(2)	0.33(12)	1.5(2)	0.73(0)

Table 4.8: Parameters for the PS→PS form factor fits following BK [7]: $\beta = 6.2$

interpolation acts like a smoothing filter over q^2 for the lattice form factor, and reduces spread at an early point in the analysis.

A pole dominance model is known to work well, and good fits are obtained. It is not surprising that the BK model for $f^{+,0}_{B\to\pi}$, a close relative of pole dominance with an extra free parameter, is similarly successful. The usefulness of the BK parameterization is in its isolation of quantities with particular theoretical significance, some of which are investigated in the next section. The fit parameters are presented in Tabs. 4.8 and 4.9.

One plausible explanation for the pattern of discrepancies between the binned $B \to \rho l\nu_l$ decay rate from Ref. [5] and this work is the existence of a large scale-setting error in q^2, which, by moving the position of the maximum in the differential decay rate, could have an effect on the event density consistent with the numbers in Tab. 4.7. Notwithstanding this possiblility, note that the numbers of Ref. [5] are themselves extrapolated from the region of high electron energy (where swamping from the Cabibbo-enhanced b→c decays is not observed) to the full kinematic range. In addition, the systematic errors on the lattice calculations are large. All things considered, the level and nature of disagreement in Tab. 4.7, while unsatisfactory, is passable, particularly when better experiments are close at hand.

	$V(0)$	M_V(GeV)	$A^{(2)}(0)$	$M_{A^{(2)}}$(GeV)
$D \to K^* l \nu_l$	0.77(5)	3.2(16)	0.69(13)	2.8(7)
$D \to \rho l \nu_l$	0.69(5)	3.3(24)	0.62(16)	3.1(14)
$B \to \rho l \nu_l$	0.97(49)	–	0.60(45)	–

	$A^1(0)$	M_{A^1}(GeV)	$A^0(0)$	M_{A^0}(GeV)
$D \to K^* l \nu_l$	0.68(3)	2.8(7)	0.61(4)	2.2(2)
$D \to \rho l \nu_l$	0.62(3)	3.1(14)	0.58(5)	2.3(2)
$B \to \rho l \nu_l$	0.46(15)	–	0.34(18)	5.5(8)

Table 4.9: Parameters for the PS→V form factor fits following pole dominance: $\beta = 6.2$

4.3 Theoretical Observations

The process of calculating heavy-light form factors on the lattice gives a number of theoretical parameters worthy of study:

4.3.1 The Coupling $g_{B^*B\pi}$

The $B^*B\pi$ coupling $g_{B^*B\pi}(q^2)$ is the dimensionless form factor defined by:

$$\langle B^*_r(p')|B(p)\pi(q)\rangle = -g_{B^*B\pi}\xi_r \cdot q(2\pi)^4\delta(p'-p-q) \tag{4.11}$$

A coupling $g_{D^*D\pi}$ is defined anologously.

At tree level in heavy meson chiral perturbation theory (HMCPT), $g_{B^*B\pi}(m_\pi^2)$ is related to the coupling $\hat{g}$ in the heavy meson chiral Lagrangian by:

$$g_{B^*B\pi} = \frac{2m_B\hat{g}}{f_\pi} \tag{4.12}$$

$g_{B^*B\pi}(m_\pi^2)$ is the physical coupling $g_{B^*B\pi}$ [46].

Crossing symmetry gives a relation to the residue of the pole 'res.' in $f^{+}_{\mathrm{B}\to\pi}(q^2)$ at $q^2 = m^2_{\mathrm{B}^*}$:

$$g_{\mathrm{B}^*\mathrm{B}\pi} = \frac{\mathrm{res.} f_{\mathrm{B}^*}}{m_{\mathrm{B}^*}} \tag{4.13}$$

$g_{\mathrm{B}^*\mathrm{B}\pi}$ can be extracted from the fit parameter c_{B} of the best fit curve for the form factor f^0, using the BK model. The estimate for the $\mathrm{B}^*\mathrm{B}\pi$ coupling $g_{\mathrm{B}^*\mathrm{B}\pi}$ is defined as follows:

$$g_{\mathrm{B}^*\mathrm{B}\pi} = 2 c_{\mathrm{B}} f_{\mathrm{B}} \tag{4.14}$$

The extraction of $g_{\mathrm{D}^*\mathrm{D}\pi}$ is performed similarly, and results are presented for these two, as well as the values of the pseudoscalar-vector-pion coupling at the unphysical quark masses input into the simulation, in Tab. 4.10, along with the HMCPT coupling constant $\hat{g}$.

$\beta = 6.2$		
κ_{heavy}	$\hat{g}$	$g_{\mathrm{H}^*\mathrm{H}\pi}$
0.1299	1.0(2)	18(4)
0.1266	0.7(1)	17(3)
0.1233	0.6(1)	17(2)
0.1200	0.51(8)	17(2)
M	$\hat{g}$	$g_{\mathrm{H}^*\mathrm{H}\pi}$
m_{B}	0.7(1)	18(3)
m_{D}	0.43(7)	32(5)

Table 4.10: The pseudoscalar-vector-pion coupling at different values of heavy meson mass. The four non-physical heavy mesons correspond to the heavy quark mass parameters used as simulation inputs.

$\beta = 6.2$			$\beta = 6.0$		
f_B	=	220(5) MeV	f_B	=	200(5) MeV
f_π	=	143(2)	f_π	=	112(3)
$f^0(q^2_{max})$	=	1.1(1)	$f^0(q^2_{max})$	=	1.2(2)

Table 4.11: Quantities relevant to the soft pion relation

4.3.2 Soft Pion Theorems

HMCPT [47] gives a soft pion theorem for $B \to \pi$ matrix elements:

$$f^0(q^2_{max}) = \frac{f_B}{f_\pi} \tag{4.15}$$

and a similar relation for $D \to \pi$ matrix elements. This family of relations has attracted considerable attention in lattice studies. On the one hand, fulfilment of this soft pion theorem is a reassurance after the extensive process of extracting form factor predictions from the lattice; when violation of this theorem is observed, however, there are many possibly revealing explanations (quenching error and poor approach to the chiral limit are the most popular). In this work, the soft pion theorem is fulfilled within the large errors, which is moderately encouraging. Hashimoto, who has been of the opinion that this soft pion theorem is violated in quenched QCD, suggests that discretization errors inherent in the relativistic simulation of heavy quarks used here may be causing a false fulfilment, an instance of two wrongs making a right [30]. This possibility may not be ruled out. Results are presented in Tab. 4.11. Preliminary results, which could have been found in Ref. [48] are superceded by those of Tab. 4.11.

$\beta = 6.2$			$\beta = 6.0$		
κ_{heavy}	M_{H}(MeV)	$f(q^2 = 0)$	κ_{heavy}	M_{H}(MeV)	$f(q^2 = 0)$
0.12000	2100(100)	0.65(5)	0.11230	2300(100)	0.66(9)
0.12330	1860(90)	0.71(5)	0.11730	2000(100)	0.70(8)
0.12660	1560(80)	0.79(4)	0.12230	1670(80)	0.77(7)
0.12990	1220(60)	0.92(3)	0.12730	1280(60)	0.86(6)

Table 4.12: $f(0)$ *vs.* heavy mass

4.3.3 Comparison with QCD Prediction for Scaling with Heavy Mass

QCD scaling dictates that the quantity $f^{+,0}(q^2 = 0, M_{\text{H}})M_{\text{H}}^{\frac{3}{2}}$ should tend to a constant in the heavy quark limit [49]. This motivates the following ansatz: [50]

$$f(q^2 = 0, M_{\text{H}}) \simeq (M_0/M_{\text{H}})^{\frac{3}{2}}(1 + \frac{X_1}{M_{\text{H}}}) \qquad (4.16)$$

Data from the four heavy quark masses of this study are tabulated in Tab. 4.12, and are presented in Fig. 4.16 together with best-fit curves from a 1-parameter fit to Eqn. 4.16, where the $f(0)$ have been extracted from a BK fit at the simulated masses. $f(0)$ at M_{D} and M_{B} are superimposed on the plot. The QCD scaling is seen to be well satisfied, and fitting to Eq$^{\text{n}}$ 4.16 gives a result for $f(0)$ at the D and B masses which is constistent that given by the procedures used in this work.

4.3.4 Measurement of the Renormalization Constants Z_{V} and b_{V}

A measurement of the renormalization constants Z_{V} and b_{V} can be made by observing that the timelike component of the flavour-degenerate lattice vector

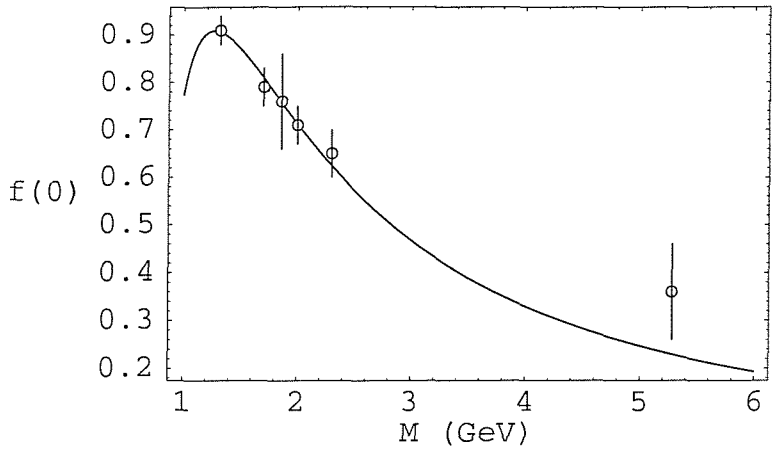

Figure 4.16: Test of QCD scaling relation for $f(0)$ ($\beta = 6.2$)

current looks like a quark counting operator. Demanding that $\langle \mathrm{P}|V_4^{\mathrm{I}}|\mathrm{P}\rangle/2m_{\mathrm{P}}$ be equal to unity for degenerate active quark in P, permits an estimate of the total multiplicative renormalization $fac. = Z_{\mathrm{V}}(1 + b_{\mathrm{V}} a\tilde{m}_{\mathrm{q}})$. This combination is tabulated in Tab. 4.13 and 4.14.

Estimates for Z_{V} and b_{V} can be extracted from a fit:

$$fac._{\kappa_{\mathrm{heavy}}} = X_0(1 + X_1 a\tilde{m}_{\mathrm{q}}(\kappa_{\mathrm{heavy}})) \tag{4.17}$$

with base points at two different values of κ_{heavy} at $\beta = 6.2$ and four different values of κ_{heavy} at $\beta = 6.0$. The results of the fit are as follows:

$$\hat{Z}_{\mathrm{V}} = X_0 = \begin{cases} 0.80(1) & \beta = 6.2 \\ 0.80(2) & \beta = 6.0 \end{cases} \qquad \hat{b}_{\mathrm{V}} = X_1 = \begin{cases} 1.25(4) & \beta = 6.2 \\ 1.27(6) & \beta = 6.0 \end{cases}$$

By comparison, the Alpha collaboration gives [51] Z_{V}, b_{V} as 0.792, 1.40(1) at $\beta = 6.2$, and 0.781, 1.47(1) at $\beta = 6.0$. The total renormalisation factor is plotted in Fig. 4.17 along with the determination of Ref. [51].

Z_{V} and b_{V} are estimated using an entirely different method to Ref. [51]. The level of agreement with Ref. [51] is one indicator that discretization error in 3pt

κ_{heavy}	$\kappa_{\text{spectator}}$	Z_{Veff}	Z_{Veff} (Alpha collab.)
0.1200	0.1346	1.29(2)	1.33
0.1200	0.1351	1.28(3)	1.33
0.1266	0.1346	1.07(2)	1.09
0.1266	0.1351	1.07(2)	1.09

Table 4.13: Multiplicative renormalisation factor for the vector current, $\beta = 6.2$. Errors in the Alpha numbers are negligible at this precision.

κ_{heavy}	$\kappa_{\text{spectator}}$	Z_{Veff}	Z_{Veff} (Alpha collab.)
0.1123	0.13344	1.57(3)	1.65
0.1123	0.13417	1.57(4)	1.65
0.1173	0.13344	1.38(2)	1.43
0.1173	0.13417	1.37(3)	1.43
0.1223	0.13344	1.20(2)	1.23
0.1223	0.13417	1.20(3)	1.23
0.1273	0.13344	1.04(2)	1.05
0.1273	0.13417	1.03(2)	1.05

Table 4.14: Multiplicative renormalisation constant for the vector current, $\beta = 6.0$. Errors in the Alpha numbers are negligible at this precision.

Green's functions may be small at $\beta = 6.2$ and not too large at $\beta = 6.0$.

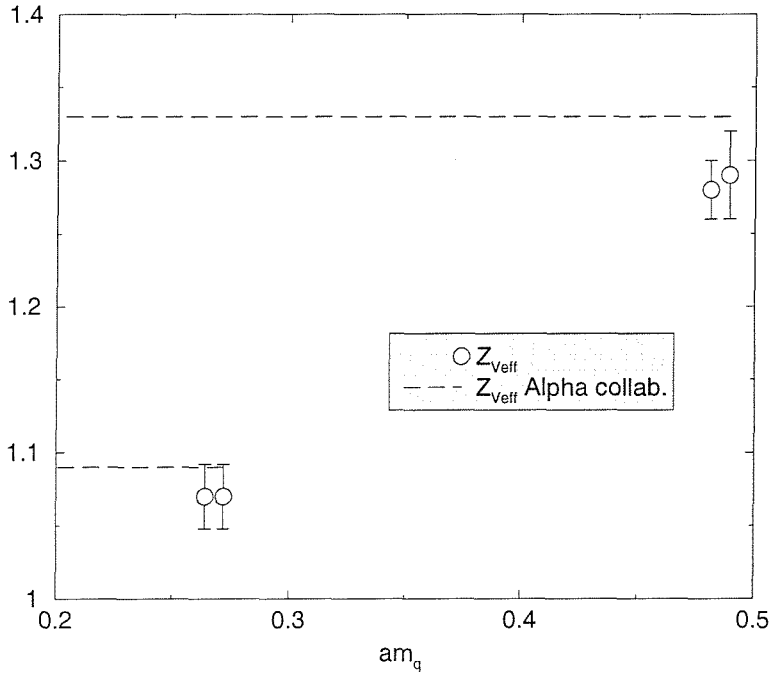

Figure 4.17: $Z_{\mathrm{V}}(1+b_{\mathrm{V}}a\tilde{m}_{\mathrm{q}})$ for different κ_{heavy} ($\beta = 6.2$). Each doublet represents a measurement from two correlators with different spectator quarks. The Alpha determinations are stretched to the left axis in order to guide the eye.

Chapter 5

Decay Constants

5.1 Results

Decay constants are presented in Tab. 5.1.

Tab. 5.2 shows the ratios of strange heavy meson decay constants to those of the light counterparts. A chiral perturbation theory approach predicts these ratios

	f_{B}(MeV)	f_{B^*}	f_{D}(MeV)	f_{D^*}
$\beta = 6.2$	220(5)	21(1)	220(3)	7.5(2)
$\beta = 6.0$	200(5)	17(2)	210(3)	6.9(2)

	f_{B_s}(MeV)	$f_{\mathrm{B}_s^*}$	f_{D_s}(MeV)	$f_{\mathrm{D}_s^*}$
$\beta = 6.2$	240(3)	20(1)	240(2)	7.3(1)
$\beta = 6.0$	210(3)	16(1)	220(2)	6.9(1)

	f_π(MeV)	f_ρ	f_{K}(MeV)	f_{K^*}	f_ϕ
$\beta = 6.2$	140(2)	3.6(3)	160(2)	3.9(2)	4.1(2)
$\beta = 6.0$	130(3)	3.4(5)	140(2)	3.6(4)	3.8(2)

Table 5.1: Decay constants, $\beta = 6.2$ and $\beta = 6.0$

	$\frac{f_B}{f_{B_s}}$	$\frac{f_{B^*}}{f_{B_s^*}}$	$\frac{f_D}{f_{D_s}}$	$\frac{f_{D^*}}{f_{D_s^*}}$
$\beta = 6.2$	0.90(3)	1.1(1)	0.91(2)	1.0(5)
$\beta = 6.0$	0.91(4)	1.1(2)	0.93(2)	1.0(5)

Table 5.2: SU(3) Ratios of decay constants, $\beta = 6.2$

to be unity at tree level, with corrections starting at second order in Λ_{QCD} over the chiral symmetry breaking scale $\mu_\chi \sim 4\pi f_\pi$.

Decay constants are inputs for the matrix elements for mixing in the B and K systems, and in estimating CKM elements from pure leptonic decay widths of mesons. Experiment has yet to measure heavy meson decay constants precisely, and so an wide range of lattice ($150 < f_B < 220$ MeV) [52, 53], and other ($f_B \to 90 - 120$ MeV [49]) calculations is tolerated in the literature. Quenched lattice calculations generally occupy the lower end ($f_B \to 150$ MeV), whereas exploratory dynamical studies give higher numbers ($f_B \to 220$ MeV). One possible reason for the high values of f_P here relative to other quenched simulations is that r_0 gives a $\simeq 10\%$ finer estimate of the lattice spacing than f_π, the usual scale-setting quantity in simulations where only the decay constants are to be extracted.

5.2 Heavy Quark Symmetry Properties

Heavy quark symmetry predicts that matrix elements of the vector and axial current bilinears obey a spin symmetry which, when combined with Eq^{ns} 3.5 and 3.6, gives the following relation between decay constants, expressed here as a function of the spin-averaged mass $\bar{M} = (m_P + 3m_V)/4$:

$$f_P f_V \overset{\bar{M}\to\infty}{\to} \bar{M} + O\left(\frac{1}{\bar{M}}\right) \tag{5.1}$$

The ratio $\tilde{U}(\bar{M})$ is defined by $\tilde{U}(\bar{M}) = \frac{f_P f_V}{\bar{M}}$. In HQET, $\tilde{U}(\bar{M}) \neq 1$ reflects deviation from the heavy quark limit. Taking up to two-loop radiative corrections into account in (continuum) HQET, $\tilde{U}(\bar{M})$ is given by [39]:

$$\tilde{U}(\bar{M}) = \left(1 + \frac{2\alpha_s(\bar{M})}{3\pi} + O(\frac{1}{\bar{M}})\right) \tag{5.2}$$

The consistency of these decay constants with continuum HQET can be tested, using a fit inspired by Eq^n 5.2:

$$\frac{f_P f_V}{\bar{M}} \sim \left(X_0 + X_1 \frac{2\alpha_s(\bar{M})}{3\pi} + X_2 O(\frac{1}{\bar{M}})\right) \tag{5.3}$$

Fig. 5.1 shows $\frac{f_P f_V}{\bar{M}}$ fit to the form specified by Eq^n 5.3, for each β. The curve for $\beta = 6.2$ is consistent with continuum HQET infinite-mass behaviour. In the case of $\beta = 6.0$, however, $O(a^2)$ corrections deflect the fitted curve from unity at infinite mass. $O(\Lambda_{QCD})$ corrections to HQET at light mass may also be partly responsible. Whatever the cause, the behaviour of $\frac{f_P f_V}{\bar{M}}$ at $\beta = 6.0$ cautions against using the results at both couplings for any systematic extrapolation to the continuum.

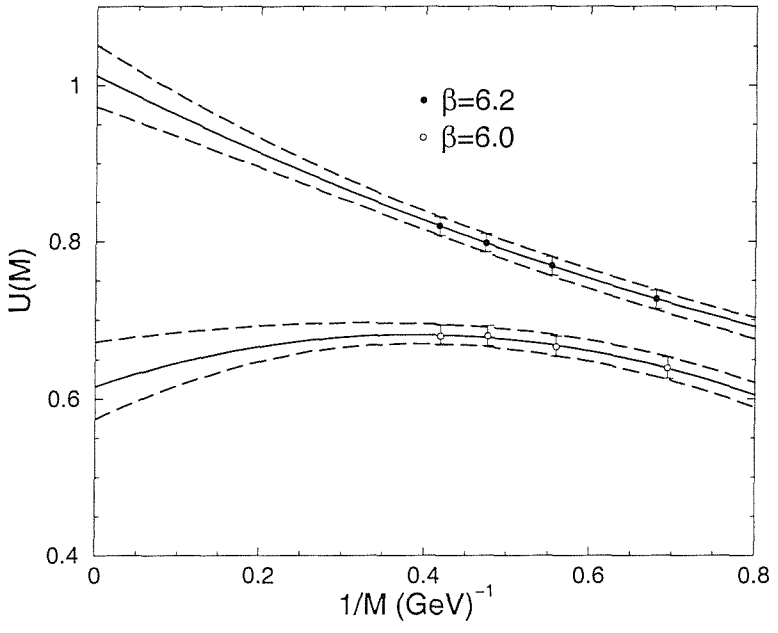

Figure 5.1: The ratio $\frac{f_P f_V}{M}$ *vs.* heavy mass

Chapter 6

Systematic Error Tables

This chapter contains only tables. A discussion is in the next chapter.

	$f^+(q^2_{\max})_{D\to Kl\nu_l}$	$f^0(q^2_{\max})_{D\to Kl\nu_l}$	f_D	f_K
Sys. error from	1.7	1.1	220MeV	160MeV
Interpolation range	1%	–	–	–
Mass scale a^{-1}	1%	1%	7%	7%
Interpolation function	25%	3%	–	–
HQET trunc. order	1%	1%	–	–
Extraction of $f_{P,V}$	–	–	–	3%
Strange quark mass	1%	2%	–	2%
Lattice difference/mass	–	–	–	1%
Coeff. c_V	2%	–	–	–
Coeff. b_A	–	–	3%	–
Composed % error	25%	4%	8%	8%

Table 6.1: Breakdown of systematic error estimates for $D \to Kl\nu_l$

	$f^+(q^2_{\rm max})_{\rm D\to\pi l\nu_l}$	$f^0(q^2_{\rm max})_{\rm D\to\pi l\nu_l}$	f_π
Sys. error from	1.4	1.5	140MeV
Interpolation range	2%	–	–
Mass scale a^{-1}	2%	2%	9%
Interpolation function	10%	–	–
Pion mass	1%	–	1%
Meson/quark chiral extr.	1%	–	–
HQET trunc. order	2%	–	–
Extraction of $f_{\rm P,V}$	–	4%	4%
Lattice difference/mass	–	1%	1%
Coeff. $b_{\rm A}$	–	3%	–
Composed % error	11%	5%	10%

Table 6.2: Breakdown of systematic error estimates for $\rm D \to \pi l\nu_l$

	$f^+(q^2_{\rm max})_{\rm B\to\pi l\nu_l}$	$f^0(q^2_{\rm max})_{\rm B\to\pi l\nu_l}$	$f_{\rm B}$
Sys. error from	8.3	1.2	220MeV
Interpolation range	1%	1%	–
Mass scale a^{-1}	3%	4%	11%
Interpolation function	365%	15%	–
Pion mass	2%	2%	–
Meson/quark chiral extr.	1%	1%	–
HQET trunc. order	13%	13%	6%
Extraction of $f_{\rm P,V}$	–	–	2%
Coeff. $c_{\rm V}$	6%	2%	–
Coeff. $b_{\rm A}$	–	–	6%
Composed % error	370%	21%	14%

Table 6.3: Breakdown of Systematic Error Estimates for $\rm B \to \pi l\nu_l$. The large variation in $f^+(q^2_{\rm max})$ is due to the proximity of $q^2_{\rm max}$ to the vector pole.

	$\|V_{cs}\|$	$\|V_{cd}\|$	$\|V_{ub}\|$
Sys. error from	0.92	0.21	0.0032
Interpolation range	–	–	1%
Mass scale a^{-1}	3%	5%	7%
Interpolation function	6%	12%	19%
HQET trunc. order	–	1%	8%
Strange quark mass	1%	–	–
Coeff. c_V	2%	2%	7%
Composed % error	7%	13%	23%

Table 6.4: Breakdown of systematic error estimates for CKM quantities

	$V(q^2_{max})_{D\to K^* l\nu_l}$	$A^2(q^2_{max})_{D\to K^* l\nu_l}$	$A^1(q^2_{max})_{D\to K^* l\nu_l}$	$A^0(q^2_{max})_{D\to K^* l}$
Sys. error from	0.94	0.93	0.77	0.89
Interpolation range	–	2%	1%	4%
Mass scale a^{-1}	4%	3%	–	2%
Interpolation function	24%	13%	7%	8%
HQET trunc. order	2%	1%	1%	4%
Strange quark mass	3%	2%	2%	3%
Coeff. c_V	5%	1%	1%	4%
Coeff. b_A	1%	1%	–	3%
Composed % error	25%	14%	7%	12%

Table 6.5: Breakdown of systematic error estimates for $D \to K^*$

	$V(q^2_{max})_{D\to \rho l\nu_l}$	$A^2(q^2_{max})_{D\to \rho l\nu_l}$	$A^1(q^2_{max})_{D\to \rho l\nu_l}$	$A^0(q^2_{max})_{D\to \rho l\nu_l}$
Sys. error from	0.88	0.97	0.71	0.81
Interpolation range	1%	2%	2%	5%
Mass scale a^{-1}	2%	1%	1%	6%
Interpolation function	37%	18%	7%	10%
HQET trunc. order	3%	3%	1%	4%
Coeff. c_V	7%	2%	1%	3%
Coeff. b_A	3%	3%	2%	23%
Composed % error	38%	19%	8%	27%

Table 6.6: Breakdown of systematic error estimates for $D \to \rho$

	$V(q^2_{\max})_{B\to\rho l\nu_l}$	$A^2(q^2_{\max})_{B\to\rho l\nu_l}$	$A^1(q^2_{\max})_{B\to\rho l\nu_l}$	$A^0(q^2_{\max})_{B\to\rho l\nu_l}$
Sys. error from	1.4	3.0	0.64	1.2
Interpolation range	2%	1%	1%	1%
Mass scale a^{-1}	3%	4%	4%	2%
Interpolation function	112%	37%	35%	115%
Meson/quark chiral extr.	–	–	–	1%
HQET trunc. order	16%	2%	21%	95%
Coeff. c_V	2%	1%	6%	39%
Coeff. b_A	22%	9%	8%	32%
Composed % error	115%	38%	42%	157%

Table 6.7: Breakdown of systematic error estimates for B $\to \rho$

	$\lvert V_{cs}\rvert_{D\to K^* l\nu_l}$	$\lvert V_{cd}\rvert_{D\to\rho l\nu_l}$	$\lvert V_{ub}\rvert_{B\to\rho l\nu_l}$
Sys. error from	0.90	0.17	0.0023
Interpolation range	2%	3%	–
Mass scale a^{-1}	1%	3%	2%
Interpolation function	3%	3%	22%
HQET trunc. order	–	3%	17%
Strange quark mass	2%	–	–
Coeff. c_V	–	1%	9%
Coeff. b_A	2%	4%	9%
Composed % error	5%	7%	31%

Table 6.8: Breakdown of systematic error estimates for CKM quantities from PS$\to$V

	f_B	f_{B^*}	f_D	f_{D^*}
Sys. error from	220MeV	21	220MeV	7.5
Mass scale a^{-1}	11%	12%	7%	10%
HQET trunc. order	6%	4%	–	–
Extraction of $f_{P,V}$	2%	5%	–	1%
Lattice difference/mass	–	1%	–	–
Coeff. c_V	–	24%	–	8%
Coeff. b_A	6%	–	3%	–
Naive/KLM norm [54]	1%	2%	–	–
Composed % error	14%	28%	8%	12%

Table 6.9: Breakdown of systematic error estimates for I=$\frac{1}{2}$ decay constants

	f_{B_s}	$f_{B_s^*}$	f_{D_s}	$f_{D_s^*}$
Sys. error from	240MeV	20	240MeV	7.3
Mass scale a^{-1}	8%	9%	6%	8%
HQET trunc. order	6%	3%	–	–
Extraction of $f_{P,V}$	–	2%	–	1%
Strange quark mass	2%	3%	2%	2%
Coeff. c_V	–	26%	–	8%
Coeff. b_A	6%	–	3%	–
Naive/KLM norm [54]	1%	2%	–	–
Composed % error	12%	28%	7%	12%

Table 6.10: Breakdown of systematic error estimates for S=1 decay constants

	f_π	f_K	f_ρ	f_{K^*}	f_ϕ
Sys. error from	140MeV	160MeV	3.6	3.9	4.1
Mass scale a^{-1}	9%	7%	–	1%	2%
Pion mass	1%	–	–	–	–
Extraction of $f_{P,V}$	4%	3%	3%	3%	3%
Strange quark mass	–	2%	–	1%	3%
Lattice difference/mass	1%	1%	–	–	–
Coeff. c_V	–	–	2%	2%	3%
Composed % error	10%	8%	4%	4%	6%

Table 6.11: Breakdown of systematic error estimates for light decay constants

	$\frac{f_B}{f_{B_s}}$	$\frac{f_{B^*}}{f_{B_s^*}}$	$\frac{f_D}{f_{D_s}}$	$\frac{f_{D^*}}{f_{D_s^*}}$
Sys. error from	0.90	0.92	0.91	0.97
Mass scale a^{-1}	2%	3%	2%	2%
HQET trunc. order	–	1%	–	–
Extraction of $f_{P,V}$	2%	3%	–	–
Strange quark mass	3%	3%	2%	2%
Lattice difference/mass	–	1%	–	–
Coeff. c_V	–	1%	–	–
Composed % error	4%	5%	3%	3%

Table 6.12: Breakdown of systematic error estimates: SU(3) ratios of decay constants

Chapter 7

Discussion of Systematic Errors

7.1 Sources of Error

Sources of error are discussed in the following order:

1. Statistical Error
2. Discretization Error
3. Finite-size Error
4. Model Errors
5. Truncation Errors
6. Parameter-fixing Error
7. Quenching Error

7.2 Statistical Error

The error bars in all figures are calculated using the bootstrap technique, using the 18^{th} and 82^{nd} percentiles of 400 resamplings as the lower and upper bound respectively. The first error on all numbers is symmetrized by setting equal to half the difference of the 18^{th} and 82^{nd} percentile.

7.2.1 The Bootstrap

The results of this work are all stochastic estimates whose underlying distribution is not accessible. They are, however, a symmetric function of the n_{cfg} identically distributed samples of some random variable. In the bootstrap procedure [55], this symmetry is used to motivate a prescription for sampling a low-bias estimate of the underlying distribution of each result: simply replace each member of the set of samples with another one chosen at random, with the possibility of repeats, and recalculate.

Any resampling does not add information, and the bootstrap prescription represents a particular degree of tradeoff between the following undesirable features:

The resampled set (bootstrap set) results are quite correlated with one another. On average, two bootstrap sets with $216 \leq n_{cfg} \leq 305$ will have at least one copy of a common 40% of the original information. Correlation must be introduced if any resampling is to retain a significant proportion of the information in the original sample. As an extreme example, filling the set with a single copy of each member of the original set bar one (selected at random) preserves almost all the information (the canonical 'jackknife').

Moreover, a bootstrap set with $216 \leq n_{cfg} \leq 305$ is expected to contain at least

one copy of only ~63% ($\overset{n_{cfg}\to\infty}{\to} 1 - e^{-1}$) of the original information (Fig. 7.1), with multiple copies filling up the rest of the space. Bias may be generally done away with by losing information at the same time; as an extreme example, filling the set with copies of exactly one member of the set chosen at random gives a very uncertain result.

Despite these features, a resampling scheme offers an *ad hoc* access to the underlying distribution of our results, without which it would be impossible either to construct error bars or to perform fits. The bootstrap is not necessarily the optimal resampling scheme for error fitting applications. However, the bootstrap has been shown to satisfy certain criteria of general applicability, and it is generally trusted for estimates of percentiles.

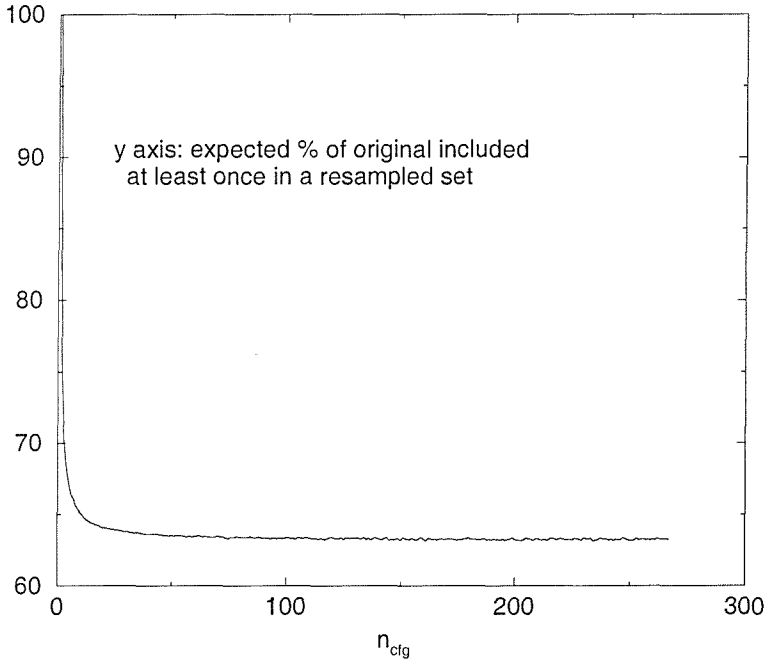

Figure 7.1: Expected percentage of n_{cfg} different members of the initial set included in a resampled set of size n_{cfg}.

7.2.2 Statistical Error in this Work

In all but the most extreme cases in this work ($B \to \rho l \nu_l$ form factors) statistics are not the most significant source of error. Otherwise put, gaining further control over extrapolation procedures is important for the future, while the lattice calculation itself is already well enough under control. Most importantly, it would appear to pay to use configurations in return for heavier quarks on a finer lattice.

7.3 Discretization Error

Discretization errors are of serious concern in this lattice simulation, since the rest masses of the heaviest lattice mesons are almost as large as the ultraviolet cutoff. The lattice dispersion relation behaves much as in the continuum, and the improvement of operators has been thoroughly implemented; these two considerations indicate that the correlation functions are largely free of discretisation error. The charge has always been that the small discretisation errors which do exist, become amplified in the extrapolation to the B scale.

The most relevant test performed in this work is to change the truncation order in the heavy quark extrapolation. The variation induced is at worst up to 15% for important quantities, which must be ascribed jointly to discretization error, model error and truncation error.

The decay constants do not scale well between $\beta = 6.0$ and $\beta = 6.2$ in this work, which is also explicable in the context of discretization error. However in light of the efforts made to reduce $O(a)$ errors, and in the absence of a continuum extrapolation, the scaling violation is tentatively ascribed to truncation error in HQET expansion, and to uncertainty in setting the scale.

An attempt is also made to take account of the uncertainty in the improvement coefficients. These are inputs into the lattice simulation, and are mostly known quite well, with exceptions being discussed in Sec. 3.1. The decay constants in particular are sensitive to the improvement coefficients.

7.4 Finite-Size Error

There are no properties of the lattice simulation in this work which are directly sensitive to the box infra-red cutoff at ~120MeV. The scales in the matrix element are sufficiently far from 120MeV that, whatever error is introduced in the chiral extrapolation, it is not regarded as being a result of simulating in a finite box.

7.5 Model Error

7.5.1 The Initial Interpolation of Lattice Data for Form Factors

In the case of interpolating the form factors in q^2, different approaches to the theory indicate a set of models, no member of which is preferred *a priori*. An interval estimate for the modeling error in a result is constructed from a spread using a representative of different reasonable classes of model. Pole dominance is an ultraviolet consideration, and is not theoretically robust in this context. The other options, which are listed in 3.7 are chosen for a combination of simplicity and smoothness.

7.5.2 General $f(q^2)$ Fits

The kinematic constraint, although analytically robust, is not used for the $A^2(q^2)$, $A^1(q^2)$, $A^0(q^2)$ fits. Implementing the kinematic constraint for these form factors is observed to cause the fit to fail. This feature is loosely attributed to the fact that the kinematic constraint cannot be implemented at exactly $q^2 = 0$ (q^2 depends on particle masses and is thus inexact), in conjunction with the general noisiness of P to V form factors. In the case of the form factors f^+ and f^0 for P$\rightarrow$P decay, this problem is not observed.

7.6 Truncation Error

The models for the extrapolation to heavy mass and light mass are infinite asymptotic series which are in practice truncated at an order somewhat smaller than the number of data points available.

The desired situation is both to have sufficient parameters to describe the substantial behaviour of the model function, and at the same time, sufficient degrees of freedom that the fit can accomodate small random fluctuations from the model. If the theory demands too many parameters, or if too few data points are available, then these desiderata may not be satisfied.

7.7 Parameter-fixing Error

Pseudoscalar decay constants, being dimensionful, are especially sensitive to the fundamental mass scale, which is the most difficult and important physical quantity to fix. (The strange and normal scales induce only a small variation in any

of the results, and the charm and bottom scales can be consistently defined.)

7.8 Quenching Error

Quenching error is not addressed systematically in this work. The agreement with experiment for $D \to Kl\nu_l$ and $D \to K^*l\nu_l$, and $|V_{cs}|$, is circumstantial evidence that quenching effects are small for these matrix elements. Once extrapolation to light mass has been performed, other model-dependent errors are large enough that quenching effects may be neglected; this is typified by the consistency with experiment, and large errors, of the determination of $|V_{cd}|$.

7.9 Do the Steps Commute?

The question of what extent the final answers are sensitive to the internal order of the analysis procedure is superficially a valid one, at least in that it suggests a variety of consistency tests. However, the systematic error bars associated with those parts of the analysis which can be interchanged, are found to be roughly symmetrical. The clear suggestion is that final numbers will be compatible with those of a permuted procedure.

Chapter 8

Conclusions

This study has produced phenomenological results of various significance. The calculation of form factors is facilitated by the smoothing of the lattice data, and by the extrapolation at constant q^2, so that statistical errors remain small in the tricky $B \to \pi l \nu_l$ case. The semileptonic form factors for decay to a vector particle are controlled to the extent of allowing extrapolations to the ρ and B masses. After extrapolation, the form factors seem to retain their expected shape, and give reasonable predictions for decay rates and for $|V_{ub}|$.

The lattice calculations of $|V_{ub}|$ from semileptonic decays cannot be said from this work to be significant in the effort to probe the consistency of the standard model. The region allowed in this work for $|V_{ub}|$ is too large and overlaps significantly both with values permitted in the standard model by current theoretical and experimental knowledge, and with values which are forbidden. However hope remains that future lattice technology for semileptonic decays may make them useful to this particular end. With so many steps in the procedure, a thorough investigation of systematic artefacts has been necessary to give any credibility to the results. The investigation of each systematic adds to the error bar, which

becomes of the order of 70% in the case of B decays and total rates. At the outset, however, it was not clear if these systematics could even be plausibly estimated, much less if that estimate would be small enough not to invalidate the procedure completely. The agreement with experiment for $D \to Kl\nu_l$ and $D \to K^*l\nu_l$, and $|V_{cs}|$ is a moderate indication that the accounting for sources of error has been thorough.

The author reflects that the next few years promise not only more computer power, but also developments in heavy quark theory, chiral perturbation theory (quenched and unquenched) and most importantly an experimental revolution in B physics.

Bibliography

[1] R.Sommer. Nucl. Phys. B411 839, 1994.

[2] M. Guagnelli et al. Nucl. Phys. B535, 389, 1998.

[3] C. Caso et al. Eur. Phys. J C3 1, 1998.

[4] J. P. Alexander et al. Phys. Rev. Lett. 77 5000, 1996.

[5] CLEO collab. B. Behrens et al. Phys. Rev. D61 52001, 2000.

[6] K. Ecklund. Proc. 8th Int. Symp. on Heavy Flavour Physics JHEP conf. proc. PRHEP-hf8/024, 1999.

[7] D. Becirevic and A. Kaidalov. hep-ph/9904490, 1999.

[8] N. Stanton. Proc. 8th Int. Symp. on Heavy Flavour Physics JHEP conf. proc. PRHEP-hf8/020, 1999.

[9] P. L. Frabetti et al. Phys. Lett. B364 127, 1995.

[10] P. L. Frabetti et al. Phys. Lett. B307 262, 1993.

[11] ALEPH collab. ALEPH 99-065 CONF 99-039, 1999.

[12] CLEO collab. Phys. Rev. D58 032002, 1999.

[13] A. Golutvin. Proc. ICHEP to be published by World Scientific, 2000.

[14] R. Feynman and A. Hibbs. Quantum Mechanics and Path Integrals Pub. Mcgraw-Hill, 1965.

[15] G. Wick. Phys. Rev. D96 1124, 1954.

[16] K. Wilson. Phys Rev D10 2445, 1974.

[17] H. B. Nielsen and M. Ninomiya. Nucl. Phys. B185 20, 1981.

[18] J. Kogut and L. Susskind. Phys. Rev. D11 399, 1975.

[19] J. Cardy. Scaling And Renormalization in Statistical Physics Pub. Cambridge, 1997.

[20] P. Mackenzie and G. Peter Lepage. Phys. Rev. D48 2250, 1993.

[21] R. Mendel and H. Trottier. Phys. Lett. B231 312, 1989.

[22] N. Isgur et al. Phys. Rev. D39 799, 1988.

[23] M. Luscher et al. Nucl. Phys. B491 323, 1996.

[24] H. J. Rothe. Lattice Gauge Theories: an Introduction, Pub. World Scentific, 1997.

[25] P. Boyle. Ph. D. Thesis, University of Edinburgh, 1997.

[26] P.Lacock et al. Phys. Rev. D51, 5403, 1995.

[27] N. Cabibbo and E. Marinari. Phys. Lett. B119 387, 1982.

[28] M. Creutz. Phys. Rev. D36 2394, 1987.

[29] C. Bernard et al. Lattice Gauge Theory: A Challenge in Large-Scale Computing Pub. Plenum, 1985.

[30] S. Hashimoto. Nucl. Phys. B, Proc. Suppl., 1999.

[31] M. Luescher and P. Weisz. Nucl. Phys. B479 429, 1996.

[32] T. Bhattacharya et al. Nucl. Phys. B, Proc. Suppl., 1999.

[33] S. Sint and P. Weisz. Nucl. Phys. B502 251, 1997.

[34] M. Guagnelli and R. Sommer. Nucl. Phys. B, Proc. Suppl., 1998.

[35] G. De Divitiis and R. Petronzio. Phys. Lett. B419 311, 1998.

[36] D. Becirevic et al. Phys Rev D60 074501, 1999.

[37] UKQCD collab. K. C. Bowler et al. Phys. Rev. D52 4905, 1995.

[38] M. Veltman. Diagrammatica Pub. Cambridge, 1994.

[39] M. Neubert. Phys. Rept. 245 259, 1994.

[40] F. Gilman and R. Singleton Jr. Phys. Rev D41, 142, 1989.

[41] J. Koerner and G. Schuler. Phys. Lett. B231 306, 1989.

[42] UKQCD collab. K. C. Bowler et al. Phys. Lett. B486 111-117, 2000.

[43] Draft P to P :UKQCD collab. K. C. Bowler et al. In preparation, 2000.

[44] Draft P to V :UKQCD collab. J. F. Gill et al. In preparation.

[45] V. Ciulli. Proc. 8th Int. Symp. on Heavy Flavour Physics JHEP conf. proc. PRHEP-hf8/044, 1999.

[46] G. De Divitiis et al. JHEP 10 010, 1998.

[47] M. Wise. Phys. Rev. D45 R2188, 1992.

[48] UKQCD collab. V. I. Lesk. Nucl. Phys. B (Proc. Suppl.) 83 313-315, 2000.

[49] V. Chernyak and I. Zhitnitsky. Nucl. Phys. B345 137, 1990.

[50] A. Abada et al. Nucl. Phys. B, Proc. Suppl 83 286, 1999.

[51] M. Luscher et al. Nucl. Phys. B491 344, 1997.

[52] GLOK collab. A. Ali Khan et al. Phys. Lett. B427 132, 1998.

[53] CP-PACS collab. A. Ali Khan et al. Nucl. Phys. B Proc. Suppl 83 265, 2000.

[54] A. El-Khadra et al. Phys. Rev D55 3933, 1997.

[55] B. Efron. Soc. for Industrial and Applied Mathematics, 1982.

[56] W. Press et al. Numerical Recipes in C, Pub. Cambridge, 1997.

[57] C. Michael and A. McKerrell. Phys. Rev. D51 3745, 1995.

Appendix A

Curve Fitting and Lattice Data

A.1 Goodness of Fit

The theoretical asymptotic behaviour of the two point Green function in Euclidean spacetime, $G_{\mathrm{MM}}(t)$ is an exponential decay with time constant equal to the energy E_{M} of the state M, the lowest-energy eigenstate of the transfer matrix:

$$G^{(2)}_{\mathrm{MM}}(t, E_{\mathrm{M}}, Z) \sim \frac{Z^2}{E_{\mathrm{M}}} e^{-E_{\mathrm{M}}T/2} \cosh(E_{\mathrm{M}}T/2) \tag{A.1}$$

The positive exponential term of the hyperbolic cosine in Eq$^{\mathrm{n}}$ A.1 arises from propagation backwards in time of a meson originating on the next period of the lattice. This is one of a number of effects, collectively referred to as lattice artefacts, which have neither physical significance nor analogues in the continuum theory. The data d_{t_i} have been averaged over field configurations. The badness of fit statistic in general use is the positive definite chi-squared statistic χ^2:

$$\chi^2(t, E_{\mathrm{M}}, Z) = \sum_{i,j \in AR} \left(G_{\mathrm{MM}}(E_{\mathrm{M}}, Z)_{t_i} - d_{t_i}\right) \mathcal{C}^{-1}_{ij} \left(G_{\mathrm{MM}}(E_{\mathrm{M}}, Z)_{t_i} - d_{t_j}\right) \tag{A.2}$$

where AR is a set of contiguous times chosen by inspection to lie the region in which asymptotic behaviour has set in. $\mathcal{C}_{ij}^{-1}$ is the inverse of the covariance matrix estimator $\mathcal{C}_{ij} = \hat{\mathrm{Cov}}(d_{t_i} d_{t_j})$. The best fit values of the parameters $\{E_{\mathrm{M}}, Z\}$, $\{E_{\mathrm{M}best}, Z_{best}\}$ are those which globally minimize the badness of fit:

$$\left.\frac{\partial \chi^2(t, E_{\mathrm{M}}, Z)}{\partial E}\right|_{E_{\mathrm{M}best}, Z_{best}} = 0 \qquad \text{(A.3)}$$

$$\left.\frac{\partial \chi^2(t, E_{\mathrm{M}}, Z)}{\partial Z}\right|_{E_{\mathrm{M}best}, Z_{best}} = 0 \qquad \text{(A.4)}$$

Minimization is performed iteratively to 10^{-6} fractional tolerance using the *amoeba* or downhill simplex method, which can be found in the Numerical Recipes books [56].

The *amoeba* routine is deterministic, and so in general cannot find a global minimum of a χ^2 function with a complicated structure of minima. Non-global minima exist generally in χ^2 when the model is a polynomial of degree $n > 2$, or a product of sums of exponentials of the parameters, as in Eq$^{\mathrm{n}}$ A.1. An initial guess is chosen by the computer in order to increase the likelihood of the a global minimum in χ^2 being found. In fact the most likely cause of an extreme badness of fit parameter is an idiosyncracy of the minimization algorithm, which can almost always be remedied by simply resetting the jump rates and directions and restarting the algorithm with the parameters which were wrongly returned. Occasionally a local minimum will be found, in which case decreasing the fit range and setting correlations between data to zero is necessary.

A.2 Correlations in the Data

The χ^2 statistic is defined so that its minimum value will occur when the parameters *e.g.* E, Z are equal to the values which correspond to a maximum in the

likelihood function $\mathcal{L}$:

$$\mathcal{L} = e^{-\chi^2(E,Z)} \tag{A.5}$$

This method requires that:

1. The data d_{t_i} are distributed multivariate normally.
2. The bias of the estimators for the means and correlation coefficients is controlled systematically.
3. The error of these estimators is reasonably small.

Michael [57] advises caution with regard to the 3rd condition, when N, the number of timeslices t_i is not much smaller than the number of samples, which is never the case here ($N_{\text{cfg}}/N \sim 20$). Conditions 1 and 2 are generally met by lattice data. The robustness of the maximum likelihood method for our data is illustrated by juxtaposing best-fit results by χ^2 minimization against best-fit results using an *ad hoc* non-parametric goodness-of-fit statistic $|V(E,Z)|$, the L_2 norm of the N-component vector V_i:

$$V_i(E,Z) = \frac{1}{n_{\text{boot}}} \sum_{nboot} \left(\frac{G_{\text{MM}}(E,Z)_{t_i} - d_{t_i,boot}}{\sqrt{\sum_i \left(G_{\text{MM}}(E,Z)_{t_i} - d_{t_i,boot}\right)^2}} \right) \tag{A.6}$$

$|V(E,Z)|$ is a number in the half-open unit interval $0 \leq |V(E,Z)| < 1$. Generally speaking, $|V(x)|$ can be thought of as a measure of by how much observation a trial point x (in this case the model function G_{MM}) is separated from an N-dimensional generalization of the median, and in one dimension, $|V(x)|$ is simply proportional to the number of of data between x and the median. A comparison of the results using χ^2 with those of $|V|$ for a typical meson correlator ($N = 16$) is presented in Tab. A.1.

	χ^2/d.o.f.	V
Best Fit E	0.841	0.843
Best Fit Z	66.0	68.2
χ^2/d.o.f.	1.10	1.53
V	0.24	0.01

Table A.1: Comparison of χ^2/d.o.f. and V badness of fit statistics for pseudoscalar mesonic green's function with quark mass parameters $\kappa_1 = 0.12, \kappa_2 = 0.13460$ at lattice coupling $\beta = 6.2$

Appendix B

Form Factor Definitions

Form factors for semileptonic meson decay in Minkowski space are defined as follows:

$$\begin{aligned}
\langle \mathrm{P}(\vec{\mathrm{k}})|\overline{\psi}\gamma^{\mu}\psi|\mathrm{P}(\vec{\mathrm{p}})\rangle &\sim \left(P^{\mu} - q^{\mu}\frac{m_{\mathrm{P}_1}^2 - m_{\mathrm{P}_2}^2}{q^2}\right) f^{+}(q^2) + \\
&\quad \left(q^{\mu}\frac{m_{\mathrm{P}_1}^2 - m_{\mathrm{P}_2}^2}{q^2}\right) f^{0}(q^2) \qquad \text{(B.1)} \\
\xi_{\nu r}\langle \mathrm{V}(\vec{\mathrm{k}})_{\mathrm{r}}|\overline{\psi}\gamma^{\nu}\gamma^{5}\psi|\mathrm{P}(\vec{\mathrm{p}})\rangle &\sim i\left(g^{\mu\nu} - \frac{k^{\mu}k^{\nu}}{m_{\mathrm{V}}^2}\right) A^{1}(q^2) - \qquad \text{(B.2)} \\
&\quad \frac{2i}{m_{\mathrm{V}} + m_{\mathrm{P}}}\left(P^{\mu}q^{\nu} - P^{\mu}k^{\nu}\frac{q\cdot k}{m_{\mathrm{V}}^2}\right) A^{2}(q^2) + \\
&\quad \frac{i(m_{\mathrm{V}} + m_{\mathrm{P}})}{q^2}\left(q^{\mu}P^{\nu} - q^{\mu}k^{\nu}\frac{P\cdot k}{m_{\mathrm{V}}^2}\right)\cdot \\
&\quad \left(A^{0}(q^2) - \frac{m_{\mathrm{P}} + m_{\mathrm{V}}}{2m_{\mathrm{V}}}A^{1}(q^2) + \frac{m_{\mathrm{P}} - m_{\mathrm{V}}}{2m_{\mathrm{V}}}A^{2}(q^2)\right) \\
\xi_{\mu r}\langle \mathrm{V}(\vec{\mathrm{k}})_{\mathrm{r}}|\overline{\psi}\gamma^{\nu}\psi\ |\mathrm{P}(\vec{\mathrm{p}})\rangle &\sim -\epsilon^{\mu\nu\lambda\rho}P_{\lambda}k_{\rho}\frac{q\cdot k}{m_{\mathrm{V}}^2} \qquad \text{(B.3)}
\end{aligned}$$

where $\mu \in \{0\ldots3\}$. P^{μ}, q^{μ}, $g^{\mu\nu}$ and $\epsilon^{\mu\nu\rho\sigma}$ are defined by the following:

$$P^{\mu} = p^{\mu} + k^{\mu} \qquad \text{(B.4)}$$

$$q^\mu = p^\mu - k^\mu \tag{B.5}$$

$$g^{\mu\nu} = \mathrm{diag}(1,-1,-1,-1) \tag{B.6}$$

$$\epsilon^{\mu\nu\rho\sigma} = \begin{cases} 1 & \Pi(\mu\nu\rho\sigma) = 1 \\ -1 & \Pi(\mu\nu\rho\sigma) = -1 \\ 0 & \text{otherwise.} \end{cases} \tag{B.7}$$

P and V denote the lowest mass pseudoscalar and vector states respectively.

Appendix C

Definitions of γ and σ Matrices

The Minkowski γ and σ matrices are defined as follows:

$$\gamma^0 = \begin{pmatrix} 1 & 0 & 0 & 0 \\ 0 & 1 & 0 & 0 \\ 0 & 0 & -1 & 0 \\ 0 & 0 & 0 & -1 \end{pmatrix} \quad \gamma^1 = \begin{pmatrix} 0 & 0 & 0 & 1 \\ 0 & 0 & 1 & 0 \\ 0 & -1 & 0 & 0 \\ -1 & 0 & 0 & 0 \end{pmatrix} \tag{C.1}$$

$$\gamma^2 = \begin{pmatrix} 0 & 0 & 0 & -i \\ 0 & 0 & i & 0 \\ 0 & i & 0 & 0 \\ -i & 0 & 0 & 0 \end{pmatrix} \quad \gamma^3 = \begin{pmatrix} 0 & 0 & 1 & 0 \\ 0 & 0 & 0 & -1 \\ -1 & 0 & 0 & 0 \\ 0 & 1 & 0 & 0 \end{pmatrix} \tag{C.2}$$

$$\gamma^5 = \begin{pmatrix} 0 & 0 & 1 & 0 \\ 0 & 0 & 0 & 1 \\ 1 & 0 & 0 & 0 \\ 0 & 1 & 0 & 0 \end{pmatrix} = i\gamma^0\gamma^1\gamma^2\gamma^3 \tag{C.3}$$

$$\sigma^{\mu\nu} = \frac{i}{2}[\gamma^\mu, \gamma^\nu] \tag{C.4}$$

The Euclidean gamma and sigma matrices $\Gamma_{1...4}$ and $\Sigma_{\mu\nu}$ are defined as follows:

$$\Gamma_i = i\gamma_i \tag{C.5}$$

$$\Gamma_4 = \gamma_0 \tag{C.6}$$

$$\Sigma_{\mu\nu} = \frac{1}{2}[\Gamma_\mu, \Gamma_\nu] \tag{C.7}$$

$$\Gamma_5 = \gamma_5 \tag{C.8}$$

Appendix D

List of Physical Inputs

Physical inputs can be found in Tab. D.1.

m_{B^0}	5279.1(12)MeV		
m_{B^*}	5324.9(18)MeV	m_{B^+}	5279.1(12)MeV
m_{D^0}	1864.6(5)MeV	m_{D^+}	1869.3(5)MeV
$m_{D^{*0}}$	2006.7(5)MeV	$m_{D^{*+}}$	2010.0(5)MeV
$m_{D_1^0}$	2422.2(18)MeV	m_{D_s}	1968.5(6)MeV
m_{K^0}	497.672(31)MeV	m_{K^+}	493.677(16)MeV
$m_{K^{*0}}$	891.66(26)MeV	$m_{K^{*+}}$	896.10(28)MeV
m_{π^0}	134.9764(6)MeV	m_{π^+}	139.56995(35)MeV
m_ρ	770.0(8)MeV		

τ_{B^0}	1.56(4)ps	τ_{B^+}	1.65(4)ps
τ_{D^0}	0.415(4)ps	τ_{D^+}	1.057(15)ps
$r(D^0 \to Kl\nu_l)$	$3.49(17) \times 10^{-2}$	$r(D^+ \to Kl\nu_l)$	$6.8(8) \times 10^{-2}$
$r(D^0 \to \pi l\nu_l)$	$3.7(6) \times 10^{-3}$	$r(D^+ \to \pi l\nu_l)$	$3.1(15) \times 10^{-3}$
$r(B^0 \to \pi l\nu_l)$	$1.8(6) \times 10^{-4}$	$r(B^+ \to \pi l\nu_l)$	–
$r(D^0 \to K^* e\nu_e)$	$1.8(6) \times 10^{-4}$	$r(D^+ \to K^* l\nu_l)$	$4.7(6) \times 10^{-2}$
$r(D^0 \to \rho l\nu_l)$	–	$r(D^+ \to \rho e\nu_e)$	$2.2(8) \times 10^{-3}$
$r(B^0 \to \rho l\nu_l)$	$2.5(9) \times 10^{-4}$	$r(D^+ \to \rho\mu\nu_\mu)$	$2.7(7) \times 10^{-3}$
		$r(B^+ \to \rho l\nu_l)$	–

$\lvert V_{cd}\rvert$	0.975(1)
$\lvert V_{cs}\rvert$	0.21(1)
$\lvert V_{ub}\rvert$	$3(2) \times 10^{-3}$
$\Lambda^{(4)}_{\overline{MS}}$	295 MeV
$\alpha_s(M_{Z^0})$	0.116(4)

Table D.1: Physical inputs: source is [3]. Masses are charge-averaged. l represents an electron or a muon, and not a tau.

Appendix E

Definitions of Improved Operators and Expressions for Improvement Coefficients

$$V_\mu \rightarrow Z_{\rm V}\left(1+b_{\rm V}a\overline{m}_{\rm q}\right)\left(V_\mu + ic_{\rm V}\partial_\nu T_{\mu\nu}\right) \tag{E.1}$$

$$A_\mu \rightarrow Z_{\rm A}\left(1+b_{\rm A}a\overline{m}_{\rm q}\right)\left(A_\mu + ic_{\rm A}\partial_\mu P\right) \tag{E.2}$$

$$\tilde{m}_{\rm q} = m_{\rm q}(1+b_{\rm M}am_{\rm q}) \tag{E.3}$$

The Alpha collaboration present improvement coefficients in polynomial or rational polynomial form:

$$Z_{\rm V} = \frac{1-0.7663g_0^2+0.0488g_0^4}{1-0.6369g_0^2} \quad \text{(Ref. [51])} \tag{E.4}$$

$$Z_{\rm A} = \frac{1-0.8496g_0^2+0.0610g_0^4}{1-0.7332g_0^2} \quad \text{(Ref. [51])} \tag{E.5}$$

$$b_{\rm V} = \frac{1-0.6518g_0^2-0.1226g_0^4}{1-0.8467g_0^2} \quad \text{(Ref. [51])} \tag{E.6}$$

$$c_{\rm A} = -0.00756 g_0^2 \frac{1 - 0.748 g_0^2}{1 - 0.977 g_0^2} \quad \text{(Ref. [23])} \tag{E.7}$$

$$c_{\rm V} = -0.01225(1) C_{\rm F} \times g_0^2 \quad \text{(Ref. [33])} \tag{E.8}$$

$$\text{where} \quad C_{\rm F} = \frac{n_{\rm c}^2 - 1}{2 n_{\rm c}} = \frac{4}{3} \quad (n_{\rm c} = 3) \tag{E.9}$$

Appendix F

An Example Set of Lattice Data

The output of the lattice simulation is presented for one combination of κ_{heavy} in Tab. F.1.

Light P		Light V		Heavy P	
m_{P}	0.281(2)	m_{V}	0.378(4)	m_{P}	0.841(1)
f_{P}	0.064(3)	f_{V}	4.2(1)	f_{P}	0.089(1)

$\lvert\vec{p}\rvert,\lvert\vec{q}\rvert,\lvert\vec{k}\rvert$	0,0,0	0,1,1	1,0,1	1,1,0	1,$\sqrt{2}$,1
f^+	–	0.88(3)	1.10(7)	1.50(6)	0.77(2)
f^0	1.00(2)	0.78(3)	0.97(6)	1.00(3)	0.69(2)
V	–	0.91(3)	0.76(15)	1.41(11)	0.84(4)
A^0	–	0.67(3)	0.85(9)	1.03(7)	0.63(3)
A^1	0.76(2)	0.61(2)	0.67(6)	0.71(4)	0.58(2)
A^2	–	0.71(7)	1.04(80)	0.90(50)	0.56(6)

$\lvert\vec{p}\rvert,\lvert\vec{q}\rvert,\lvert\vec{k}\rvert$	0,$\sqrt{2}$,$\sqrt{2}$	1,1,$\sqrt{2}$	1,$\sqrt{3}$,$\sqrt{2}$	1,2,1
f^+	0.58(4)	0.50(6)	0.73(5)	0.66(3)
f^0	0.58(4)	0.52(5)	0.68(6)	0.68(3)
V	0.53(6)	0.41(7)	0.41(9)	0.66(6)
A^0	0.43(2)	0.37(2)	0.53(4)	0.42(3)
A^1	0.38(3)	0.31(3)	0.48(5)	0.52(3)
A^2	0.26(5)	0.16(5)	0.48(13)	0.52(5)

Table F.1: Output of the lattice simulation at for $\kappa_{\mathrm{heavy}} = 0.12$, $\kappa_{\mathrm{light}} = 0.1346$, $\kappa_{\mathrm{spectator}} = 0.1346$, $\beta = 6.2$: masses, decay constants and form factors. Momenta are to be multiplied by $\frac{\pi}{12}$